Morphology of contorted fluid structures

Christophe Dumouchel, F Thiesset, Thibaut Ménard

Morphology of contorted fluid structures

C. Dumouchel[a], F. Thiesset[a], T. Ménard[a]

[a]*CNRS, Normandy Univ., UNIROUEN, INSA Rouen, CORIA, 76000 Rouen, France*

Abstract

Multiphase flows reveal contorted fluid structures which cannot be described in terms of drop/bubble diameter distribution. Here we use a morphological descriptor which originates from the field of heterogeneous materials that was proved to be nicely tailored for characterizing the microstructure of e.g. porous media. It is based on the Minkowski Functionals - an erudite expression which simply designates the integrated volume, surface, mean and Gaussian curvatures - of all surfaces parallel to the liquid-gas interface. We here apply this framework to different multiphase flow systems and prove that the Minkowski Functionals are effective for providing insights into their morphodynamical behavior.

Keywords: Multiphase flows, Interface, Topology, Morphology, Geometry

1. Introduction

Liquid atomization in multiphase flows is one example of physical mechanism whose investigation has to consider the morphodynamics of the involved fluid structures. This process is multi-scale since some physical phenomena such as surface tension and viscous damping may act at very different time and spatial scales than other phenomena such as deformation due to turbulent straining. Since liquid atomization aims at increasing the area between the two phases, the following up of the interface during time imposes itself to investigate its dynamics. However, the task is not easy because, as evidenced by the numerous visualizations in the literature, atomizing liquid flows have complex shapes [5, 19, 20, 32, 34]. Hence, a complete description of multiphase flow cannot encompass describing the dynamical behaviour of liquid structures with different morphology.

During the flow deformation, perturbations of different origin favor the growth of liquid structures of different sizes and shapes, and showing contracting (bottle neck) and accumulating (swelling) regions prefiguring possible breakup events. The multi-scale nature of these systems require to be accounted in the description of the mechanism to make possible the prediction of breakup events and, therefore, of the drop size distribution of the final spray.

The literature dedicated to the description of liquid-gas flows reports the existence of different approaches: the Volume-based Scale Distribution (VSD) [9], the Surface Curvature Distribution (SCD) [5, 13] and the two-point structure functions of the phase indicator field [31, 32, 34]. Inspired by the fractal dimension measurement technique based on the Euclidean Distance Mapping method, the VSD provides the volume comprised between the liquid-gas interface and the surface parallel to it and at a distance $d/2$ in the liquid phase. This parallel surface delimits the system resulting from the d-scale erosion of the liquid system. The scale derivative of the VSD is proportional to the surface area of the eroded system. The variations of the VSD and of the eroded system surface with time and scale inform on the liquid structure morphology and give access to its dynamics.

The approach based on the structure functions of the phase indicator function is due to [31, 32, 34]. This theory shares some similarities with the analysis of Lu and Tryggvason [19, 20] based on the correlation function of the phase indicator. It relies on the machinery of two-point statistical equations which originates from the single-phase turbulence community. Interestingly, [32, 34] noticed that two-point statistics of the

*CNRS, Normandy Univ., UNIROUEN, INSA Rouen, CORIA, 76000 Rouen, France
Email: christophe.dumouchel@coria.fr (C. Dumouchel)
Email: fabien.thiesset@coria.fr (F. Thiesset)
Email: thibaut.menard@coria.fr (T. Ménard)

phase indicator are also widely used for characterizing the microstructure of porous media [1, 7, 36, to cite only but a few], colloids [16], or fractal aggregates [27]. Many key analytical results were obtained notably to link the small-scales expansions of the two-point correlations to some geometrical characteristics of the interface (surface area and curvatures) [3, 6, 30]. In [31, 32, 34], the analysis of two-point statistics is supplemented by a transport equation allowing the space and scale dynamics of the flow to be probed.

The SCD [5, 13] finds its foundation of some results of differential geometry and reads as a joint probability distribution density function of finding the mean and Gaussian curvatures at some point on the liquid-gas interface. Together with the distributions of surface area and liquid volume, a more complete set of geometrical metrics for characterizing objects of any shapes is expected with the SCD. Introducing the mean and the Gaussian curvatures allows defining the local characteristic scales of the interface as the local radius of curvature. In a recent study [25], the SCD was used in conjunction with the information provided by the liquid volume fraction and surface density (the ELSA model) to provide early predictions of the spray drop size distribution.

As suspected by [5], the VSD and SCD approaches are connected to each other. This has been mathematically established in a previous work [33]. It is demonstrated that the successive scale derivatives of order 1 to 3 of the VSD $V(d)$ represent the surface area $S(d)$ of the eroded system, its area-weighted-average mean curvature $H(d)$ and its area-weighted-average Gaussian curvature $G(d)$, respectively. Valid for the small scale range only, this result underlines the importance of the four quantities $V(d)$, $S(d)$, $H(d)$ and $G(d)$ to describe the system. These quantities turn out to be the system Minkowski Functionals (MFs), a notion issuing from the integral geometry.

The MFs constitute a family of morphological descriptors that describe not only the content (area) but also topology (connectivity), and shape (geometric curvature) of the system [21]. They benefit from an extensive literature dedicated to porous media, fluctuating interface, image analysis [2, 21, 23]. The MFs generalize curvature integrals over smooth surface to the case of surfaces with singular edges and corners [2] and, when combined with the morphological concept of parallel surfaces, can be used to characterize and model complex spatial structures [23]. Although widely employed in porous media, the only study we are aware of which makes use of Minkowski Functionals in multiphase flows is the one due to Tryggvason and Lu [37]. Note that in the latter study, the MFs were computed only for the liquid-gas interface but not studied for the different parallel surfaces.

The purpose of the present work is to evaluate the potential of the MFs to provide a general description of the flow structures morphology in multiphase flows. This paper follows along the line of one of our previous works [33]. The MFs rely on some mathematical foundation originated from integral and differential geometry. Hence, the present paper ineluctably presents some relatively abstract concepts and mathematical technicalities which we try to expose in a handy manner. The present paper is organized as follows. Section II introduces the MFs and their application to parallel surfaces. Most mathematical technicalities are detailed in the appendix while the main core of the text resumes the essential results a general reader should retain. Section III provides applications of the MFs to multiphase flows. Three simple situations are first considered: an oscillating drop (with no breakup events), a relaxing ligament (with breakup events) and the Rayleigh-Plateau instability of a cylindrical ligament of liquid. Then the framework is used to explore more complex situations: two-phase homogeneous isotropic turbulence and a turbulent liquid jet flow issuing from the triple disc injector. Conclusions are drawn in a last section.

2. Theoretical considerations

2.1. The Minkowski functionals and their relation for convex bodies

The Minkowski functionals designate four geometric measures of a given body with surface $\mathcal{S}$ (in our case, $\mathcal{S}$ is simply the liquid gas interface):

- the volume V enclosed by the surface $\mathcal{S}$
- the surface area S defined by:

$$S = \int_{\mathcal{S}} dS \tag{1}$$

- the area integrated mean curvature H:

$$H = \int_{\mathcal{S}} \frac{1}{2}(\kappa_1 + \kappa_2) dS \tag{2}$$

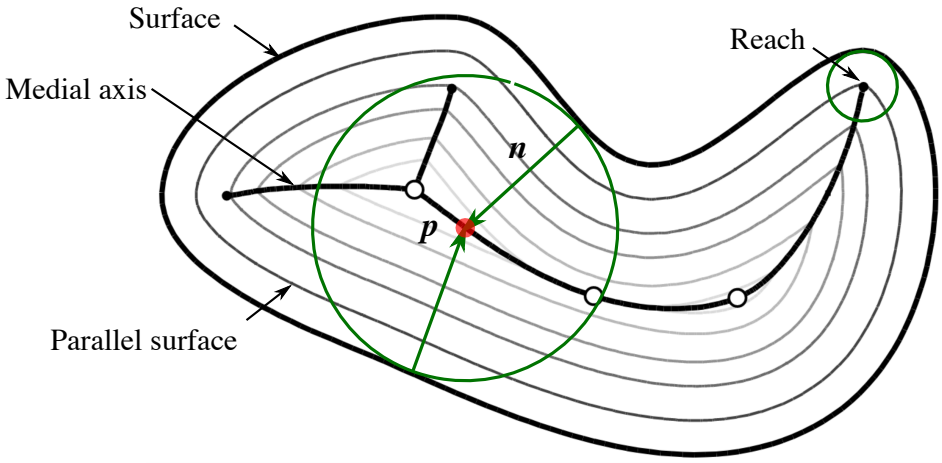

Figure 1: Graphical representation of the original body and its parallel surfaces. The medial axis and the reach of a surface are also shown

- the area integrated Gaussian curvature G

$$G = \int_{\mathcal{S}} \kappa_1 \kappa_2 dS \tag{3}$$

where dS is an elementary surface element, and κ_1, κ_2 are the two principal curvature component. By virtue of the Gauss-Bonnet theorem, for a closed surface, the area integrated Gaussian curvature G is related to the Euler characteristic χ by

$$G = 2\pi\chi \tag{4}$$

χ is a topological invariant, i.e. it depends only on the topology of the body under consideration, regardless of the way it is bent. For instance $\chi = 2$ for a sphere and for any other body homomorphic to a sphere, e.g. a spheroid. $\chi = 0$ for a cylinder and for any other homomorphic bodies to a cylinder (extruded systems). The MFs are sometimes referred to as integral geometric measures since they are obtained after integration over the surface $\mathcal{S}$. They have interesting properties, the most important are probably that they are additives (the MFs of an ensemble of body is the sum of their respective MFs) and they are invariant upon translation and rotation of the body. Therefore, a system constituted of N spheroids has $\chi = 2N$, irrespective of their relative positions and orientation.

The literature of heterogeneous material [2, 21, 23] indicates that it is worth defining and characterizing the MFs not only for the body itself but for bodies that are obtained upon dilation or erosion of the original system. The set of systems that are formed upon dilation or erosion of the original system at scale d form an infinite set of parallel bodies, i.e. their surface is distant to the original surface $\mathcal{S}$ by a distance $d/2$ in the surface normal direction. Such parallel surfaces are shown in Fig. 1.

The MFs of all parallel bodies constitute a set of morphological descriptors of the actual system. The main purpose of the present section is to provide theoretical insights into the distribution of V, S, H and G as a function of the erosion scale d. Note that in previous work by the same authors [9], only $V(d)$ and some of its derivatives with respect to d were studied. Here we generalize the approach by considering the other three MFs.

The question we will address here is how to relate the MFs at a given scale d to the MFs of the original system (at $d = 0$). Such relations were derived in [33], where it reads:

$$V(d) = V(0) - S(0)\frac{d}{2} - H(0)\frac{d^2}{4} - G(0)\frac{d^3}{24} \tag{5a}$$

$$S(d) = S(0) + H(0)d + G(0)\frac{d^2}{4} \tag{5b}$$

$$H(d) = H(0) + G(0)\frac{d}{2} \tag{5c}$$

$$G(d) = G(0) \tag{5d}$$

For readers who may be interested, the derivations are reproduced in Appendix A.2 using tools from differential geometry (the geometry of twice differentiable surfaces).

Eqs. (5) reveal that the MFs at scale d are related to the MFs of the original system by simple polynomial formulas. In other words, only the MFs at scale $d = 0$ are needed to estimate the MFs at a given erosion scale d. In addition, from Eqs (5), it is easy to show that

$$-2V(d)_{,d} = S(d) \tag{6a}$$
$$S(d)_{,d} = H(d) \tag{6b}$$
$$2H(d)_{,d} = G(d) \tag{6c}$$

where $\bullet_{,d}$ denotes the derivative with respect to d. Eqs. (6) show that the MFs are related to each other by successive derivatives with respect to the erosion scale d. In other words, $S(d)$, $H(d)$, $G(d)$ can simply be deduced from the knowledge of $V(d)$ only.

In Appendix A.3, we also show that the same hold true for non differentiable surfaces such as triangulated surfaces. This is particularly convenient since numerically, the surfaces one has to deal with fall within such category. In this situation, the derivations resort to some tools from integral geometry (the geometry of continuous but non differentiable surfaces). Again, the mathematical technicalities are gathered in Appendix A.3 to whom may be interested.

In Fig. 3, we show an example of MFs for an ellipse (the leftmost figure of Fig. 2) as a function of the erosion scale d. More details about the parameters of this ellipse and the numerical method for computing the MFs will be given later in this section. We see that the volume $V(d)$ is a decreasing function of d which reaches zero when the erosion scale attains the maximum erosion scale (the scale at which the system is fully eroded). The maximum erosion scale thus plays an important role. The surface $S(d)$ follows the same trend. We further note that the equality $S(d) = -2V(d)_{,d}$ applies very nicely for all erosion scales. The Euler characteristic $\chi(d)$ is zero everywhere since the ellipse shown in Fig. 2 is homomorphic to a cylinder (the Gaussian curvature is zero everywhere on the surface since $\kappa_2 = 0$). What is the most important in Fig. 3 is that the relation $H(d) = S(d)_{,d}$ appears to hold only for small values of d while systematic deviations appear for scales beyond a certain transition value $d \gtrsim 0.35$ times the maximum erosion scale. This means that Eqs. (5) and (6) apply only over a limited range of scales and some corrections might be needed in general situations. Since for scales smaller than this transition value, the MFs of the original surface allow the MFs at d to be deduced, generalizing the MFs to the different eroded bodies does not provide any other informations than the one deduced from the original system. The MFs of parallel surfaces start providing supplementary informations for scales larger than this transition scale. This leads [2] to state "the Minkowski functions of the parallel body contains more information about the spatial structure than just the MFs at zero dilation. [or erosion]. The parallel body [...] depends in turn on non-local properties such as narrow throats or bottle necks."

It is worth discussing the source leading to the discrepancy between Eqs. (6) and the results shown in Fig. 3. As shown in Fig. 1, for some sufficiently large distance $d/2$ from the original surface, a point on the eroded surface might have more than one closest neighbor on the original surface. This is the case for example for point $\boldsymbol{p}$ represented by the red dot in Fig. 1. The point $\boldsymbol{p}$ is also the center of the bi-tangent circle, i.e. the circle that is locally tangent to at least 2 points on the original surface. The set of points for which this occurs forms the medial axis which is also displayed in Fig. 1. The minimum radius of the set of bi-tangent circles is called the **reach** of the system. As shown in Appendix B, for scales beyond the reach, some cusps are forming on the parallel surfaces and therefore Eq. (5) and (6) ceases to apply. Thus, the reach is an important notion since it separates the range of erosion scales for which the system can be described using only geometric measures (the MFs at scale $d = 0$) and the range of scales where the MFs start being a morphological descriptor thereby providing information not only about the geometry, but also about the structure.

2.2. Extension to scales beyond the reach

We just have highlighted that the MFs start being important measures about the system morphology when the erosion scale goes beyond the reach of the system. In order to better understand the informations carried by the MFs about the system morphology, we now provide corrections to Eqs. (6). We have considered two families of shapes that are displayed in Fig. 2:

- Extruded systems, which are obtained by translating a plane curve into the third directions. In particular, we consider the two leftmost shapes in Fig. 2, i.e. an extruded ellipse and an extruded

Cassini oval. Since $\kappa_2 = 0$ everywhere on the surface, these systems are homomorphic to a cylinder, i.e. their Euler characteristic is zero. The volume (surface area) of such systems is given by the covered area (delineated perimeter) multiplied by the extrusion length.

- Object of revolution, which are obtained by rotating a plane curve along a given axis. In particular, we consider the two rightmost shapes in Fig. 2, i.e. a prolate spheroid (rotation with respect to the ellipse major axis) and an oblate spheroid (rotation with respect to the ellipse minor axis). We have chosen these two situations because of their different medial axis. Indeed, the medial axis of prolate spheroids is a line which is co-linear with the ellipse major axis while the one of oblate spheroids is a circle perpendicular to the ellipse minor axis.

For all such systems, one can derive general expressions similar to Eqs. (6) but which hold irrespective of d. In case of one cusp event, one can write:

$$-2V(d)_{,d} = S(d) \tag{7a}$$
$$S(d)_{,d} = H(d) - l_c C_2(\theta) \tag{7b}$$
$$2H(d)_{,d} = 2\pi\chi(d) + 2\pi C_3(\theta) \tag{7c}$$

Here, l_c is the length of the cusps that are formed at a given erosion scale. C_2 and C_3 are two corrections that depends on θ defined as the angle between the surface normal and the medial axis. It depends implicitly on d. Due to the additivity property of MFs, the correction to be made when multiple cusp events occur for the same erosion scale is the sum of the corrections for each cusp event.

Table 1 compiles the expression for cusp length l_c and corrections C_2, C_3 for the aforementioned types of system. $C_2(\theta)$ and $C_3(\theta)$ emphasize that the relation between the MFs beyond the reach depend on local (not only integral) properties of the interface.

Table 1: Corrections l_c, C_2 and C_3 appearing in Eqs. (7)

	Extruded system	Axisym. syst. lin. axis	Axisym. syst. circ. axis
l_c	h	-	$2\pi r_c$
$C_2(\theta)$	$\tan\theta - \theta$	-	$\tan\theta - \theta$
$C_3(\theta)$	0	$\frac{(1-\cos\theta)^2}{\cos\theta}$	$\frac{\theta}{\cos\theta} - \sin(\theta)$

The derivations for such corrections are given in the Appendix. The extruded systems are treated Appendix B.2 while the bodies of revolution with linear and circular medial axis are tackled in Appendix B.3 and §Appendix B.4, respectively.

Eqs. (7) and table 1 indicate that irrespective of the shape under consideration, the relation $-2V(d)_{,d} = S(d)$ remains valid. This result is rather general and may hold for even more complex morphology than the one presented here. The correction C_3 appears to be zero for extruded systems, while the correction $l_c C_2$ is absent for bodies of revolution characterized by a linear medial axis (such as a prolate spheroid). Finally, both $l_c C_2$ and C_3 contribute for surface of revolution with circular medial axis (such as a oblate spheroid). Therefore, looking specifically at the difference between $H(d)$ ($G(d)$) and $S(d)_{,d}$ ($2H(d)_{,d}$) allows us to discriminate between the different shapes and assess if the structure under consideration is rather extruded (only $l_c C_2$ contributes), elongated (as for prolate spheroid in which case only C_3 contributes) or flatten (as for oblate spheroid where both $l_c C_2$ and C_3 contribute). Further, the scales at which such corrections contribute are also very important since they provide useful informations about the size of narrow-throats or bulges. To provide more insights into the appropriateness of Eqs. (7) and the behaviour of $l_c C_2$ and C_3, we now numerically estimate the MFs for the four shapes presented in Fig. 2.

2.3. Numerical assessment

In all situations, an approximation of the level-set function is first initialized before proceeding to the re-initialization algorithm of [29] to ensure that the different level-set form parallel surfaces. For this purpose,

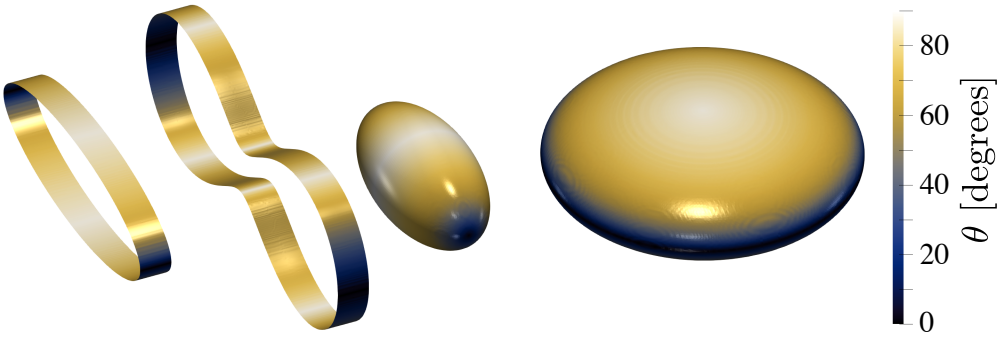

Figure 2: Representation of the different validation test cases. From left to right, the extruded ellipse, the extruded Cassini oval, the prolate spheroid and the oblate spheroid. The surfaces are coloured by the angle θ

we use the ARCHER code [24, 38] which will be described in further details later in this paper. The volume $V(d)$, surface area $S(d)$, mean $H(d)$ and Gaussian curvatures $G(d)$ for each level-set $d/2$ are computed using the method of [8, 13] which has the main advantage of incorporating a topological constraint in the curvature calculation (the Gauss-Bonnet theorem). We use prior versions of the routines now available through the Mercur(**v**)e project [1].

To obtain the set of points of the medial axis, we compute for each vertex on the triangulated zero level-set surface, the location of the intersection between the normal issuing from this vertex and either the xz-plane for extruded systems, the x axis for axisymmetric objects with linear medial axis or xy plane for axisymmetric objects with circular medial axis. Then, the angle θ and distance from the medial axis can be readily computed using trivial trigonometry. For each scale $d/2$, we sum the contribution $l_c C_2, C_3$ of all vertex whose distance from the medial axis falls within an interval $d/2 - \Delta d/2 : d/2 + \Delta d/2$. Δd was chosen sufficiently small for not loosing some scale dynamics and sufficiently large to ensure statistical convergence. Generally, 150 to 200 points for the scale parameter $d/2$ were prescribed, ranging from zero to the maximum erosion scale (i.e. the scale beyond which the system is fully eroded).

The four validation shapes coloured by the angle θ are depicted in Fig. 2 and are discussed below.

2.3.1. The extruded ellipse

We start by validating Eq. (7) for an extruded ellipse whose major axis a aligns with x and its minor axis b aligns with y. We chose $a/b = 10/3$ and h was set arbitrarily to $h = b/1.6$. The reach of such a surface is given by $b^2/a = 0.3b$ and hence we expect corrections to be non zero for scales $d/2 > 0.3b$.

Results are portrayed in Fig. 3. The scale parameter d is normalized by $\mathcal{D} = 2b$ and the geometrical properties $V(d)$, $S(d)$, $H(d)$ are normalized by their respective values at $d = 0$. We observe that the correction operates only on $H(d)$ and, as expected, $l_c C_2$ starts being non-zero for scales $d/\mathcal{D} > 0.3$. The correction appears to increase with increasing scales since θ increases from 0 (for point located around $y = 0$, see Fig. 2) to 90^o (for points around $x = 0$, see Fig. 2). For scales d larger than $\mathcal{D} = 2b$, the system has been entirely eroded and hence $V(d > \mathcal{D}) = S(d > \mathcal{D}) = H(d > \mathcal{D}) = \chi(d > \mathcal{D}) = 0$. The different curves presented in Fig. 3 emphasize that Eq. (7) holds very nicely for all scales. This validates our calculation and proves in particular that the assumption about the triangle OAB holds very nicely.

2.3.2. The extruded Cassini oval

Analytical results for extruded bodies are further confronted to numerical data for a Cassini oval. The later is parametrized with the location of the foci a aligned with the x axis, and the shape parameter b which were chosen in such way that $b/a = 150/148$. The scale d which ought to be reached for the Cassini oval to be fully eroded is the size of the bulge and is equal to $\mathcal{D} = b^2/a$. The reach for such a parametrization of the Cassini oval is equal to half the size of the neck and is given by $(b^2 - a^2)^{1/2}$. Hence, we then expect the correction $l_c C_2$ to be non-zero for scales $d \gtrapprox 0.32\mathcal{D}$.

Fig. 4 depicts the volume $V(d)$, surface area $S(d)$, mean curvature $H(d)$ and Euler characteristic $\chi(d)$ for the Cassini oval. We find again that the correction appears only at the level of $H(d)$ while the classical Steiner formula applies to $S(d)$ and $\chi(d)$. The correction $l_c C_2$ starts being active for scales $d \gtrapprox 0.32\mathcal{D}$ and brings

[1] http://docs.mercurve.rdb.is/

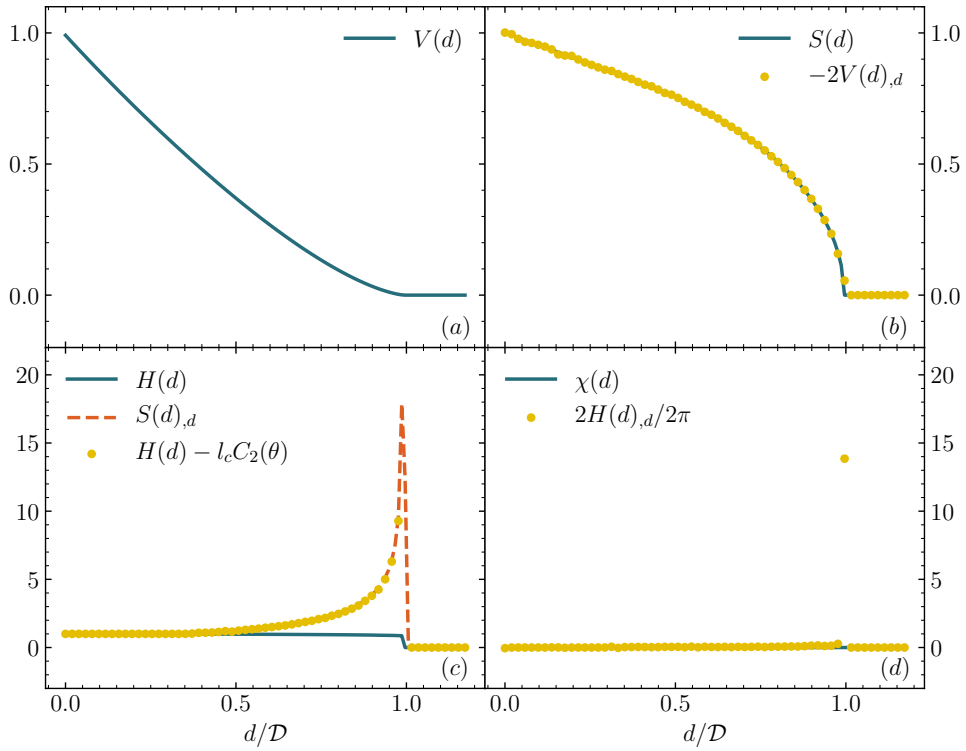

Figure 3: (a) Volume $V(d)$, (b) surface area $S(d)$, (c) mean curvature $H(d)$ and (d) Euler characteristic $\chi(d)$ as a function of the erosion scale d for the extruded ellipse.

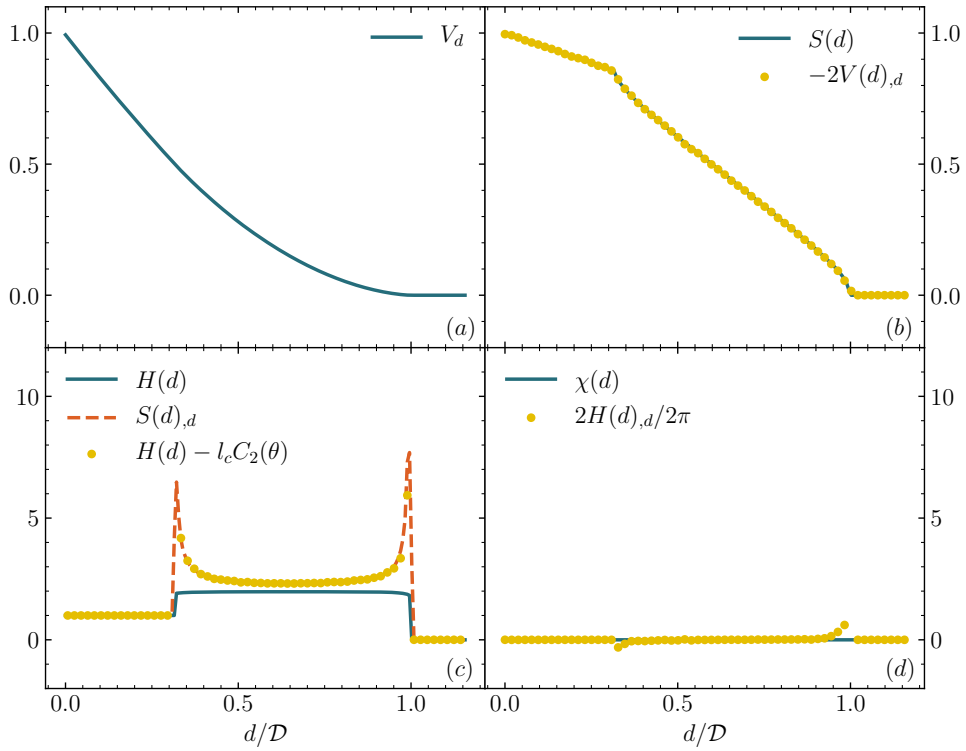

Figure 4: (a) Volume $V(d)$, (b) surface area $S(d)$, (c) mean curvature $H(d)$ and (d) Euler characteristic $\chi(d)$ as a function of the erosion scale d for the extruded Cassini oval.

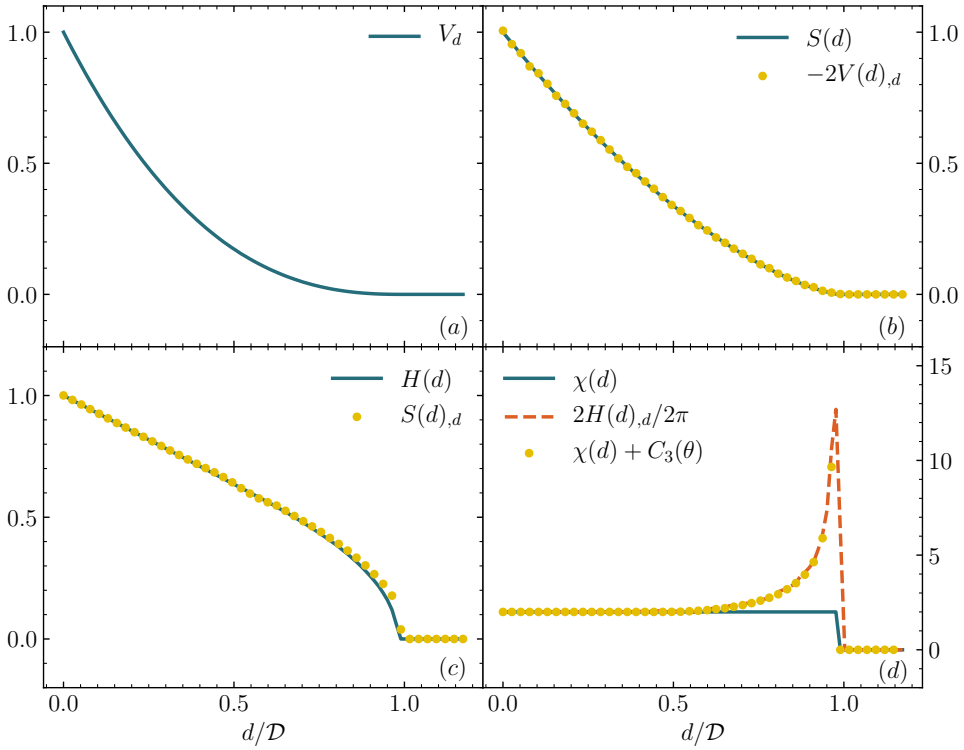

Figure 5: (a) Volume $V(d)$, (b) surface area $S(d)$, (c) mean curvature $H(d)$ and (d) Euler characteristic $\chi(d)$ as a function of the erosion scale d for the prolate spheroid

the necessary complement to represent the scale evolution of $S(d)_{,d}$. We note two peaks in the correction $l_c C_2$, one located at the reach and another located at $\mathcal{D}$. These two peaks are due to the contributions of the neck and the bulge, respectively, where $\theta \to \pi/2$ and hence $C_2 \to \infty$ (see Fig. 2). The value of $H(d)$ between these two peaks indicates that the eroded system becomes the union of two disconnected systems.

It is worth noting that, in general, the correction $l_c C_2$ should be summed over the number of cusps present in a given eroded system, the latter could possibly vary with respect to the erosion scale.

2.3.3. The prolate spheroid

We push further the validation of Eq. (7) to a body of revolution with a linear medial axis. For this purpose, is considered a prolate ellipsoid obtained by rotating the same ellipse as before around the x-axis. We have again $a/b = 10/3$ and thus the reach is equal to $0.3b$ while the scale d eroding completely the system is $\mathcal{D} = 2b$.

In agreement with Eqs. (7), Fig. 5 evidences that the correction $l_c C_2$ is zero while the correction C_3 allows $H(d)_{,d}$ to be accurately represented. C_3 starts to contribute for scales d larger than $0.3\mathcal{D}$, as expected. When d increases, the correction C_3 increases before reaching a peak at $d = \mathcal{D}$ where $\theta = \pi/2$ and hence $C_3 \to \infty$.

2.3.4. The oblate spheroid

The last validation test concerns a body of revolution with a circular medial axis. Here, we consider the rotation of the same ellipse but around the y axis, thereby forming an oblate spheroid. The reach and maximum erosion scales are the same as the prolate spheroid.

Fig. 6 reveals that the correction appears on both $H(d)$ and $\chi(d)$ while the classical Steiner formula applies to $S(d)$. $l_c C_2$ and C_3 operate for scales $d > 0.3\mathcal{D}$ as expected. Eqs. (7) with $l_c C_2$ and C_3 given in Table 1 hold very nicely for all scales considered. This confirms that the analysis performed in §Appendix B.4 is valid.

3. Application to multiphase flows

The analysis is now applied to real systems. Here we focus on the ability of parallel sets to provide insights into the morphology of deformed liquid structures evolving in a gaseous atmosphere, with particular

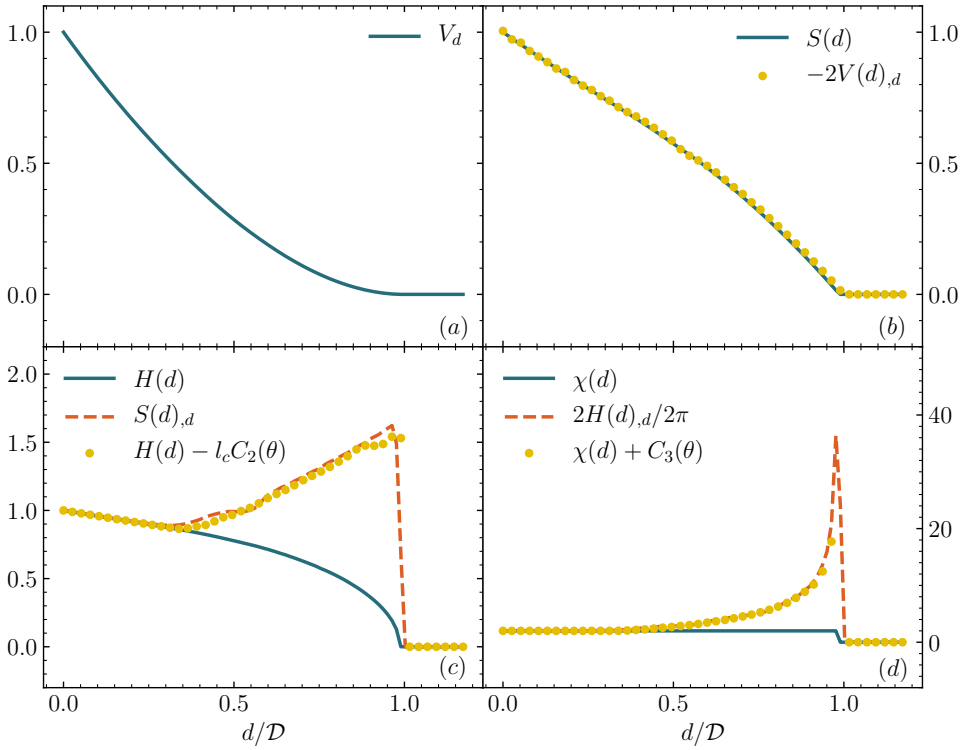

Figure 6: (a) Volume $V(d)$, (b) surface area $S(d)$, (c) mean curvature $H(d)$ and (d) Euler characteristic $\chi(d)$ as a function of the erosion scale d for the oblate spheroid

emphasis on an oscillating droplet, an elongated ligament and the Plateau-Rayleigh instability. We will also address turbulent flows, namely a liquid-gas homogeneous isotropic turbulence and a turbulent jet issuing from the triple-disc injector. The latter case will be analysed using experimental data whilst all other configurations are explored using numerical data obtained by the code ARCHER which is presented below.

3.1. Description of the ARCHER code

Numerical data of liquid/gas flows are gathered using the High-Performance-Computing code ARCHER developed at the CORIA laboratory [24]. It is based on the one-fluid formulation of the incompressible Navier-Stokes equation which is solved on a staggered Cartesian mesh, viz.

$$\begin{aligned} \partial_t\ \rho\boldsymbol{u} \quad &+ \quad \boldsymbol{\nabla}\cdot(\rho\boldsymbol{u}\otimes\boldsymbol{u}) = \\ &- \quad \boldsymbol{\nabla}p + \boldsymbol{\nabla}\cdot(2\mu\boldsymbol{D}) + \boldsymbol{f} + \gamma\mathcal{H}\delta_s\boldsymbol{n}. \end{aligned} \tag{8}$$

p is the pressure field, $\boldsymbol{D}$ the strain rate tensor, $\boldsymbol{f}$ a source term, μ the kinematic viscosity, ρ the density, γ the surface tension, $\boldsymbol{n}$ the unit normal vector to the liquid-gas interface, $\mathcal{H}$ its mean curvature and δ_s is the Dirac function characterizing the location of the liquid gas interface. For solving Eq. (8), the convective term is written in conservative form and solved using the improved [26] technique presented in [38]. The method of [28] is used to compute the viscous term. To ensure incompressibility of the velocity field, a Poisson equation is solved. The latter accounts for the surface tension force and is solved using a MultiGrid preconditioned Conjugate Gradient algorithm (MGCG) [42] coupled with a Ghost-Fluid method [15].

A coupled level-set and volume-of-fluid (CLSVOF) solver is used for transporting the interface, the level-set function accurately describing the geometric features of the interface (its normal and curvature) and the volume-of-fluid function ensuring mass conservation. The density is calculated from the volume-of-fluid (or liquid volume fraction) as $\rho = \rho_l\phi + \rho_g(1-\phi)$, where ρ_l, ρ_g is the density of the liquid and gas phase. The dynamic viscosity (μ_l or μ_g) depends on the sign of the Level Set function. In cells containing both a liquid and gas phase, a specific treatment is performed to evaluate the dynamic viscosity, following the procedure of [28]. For more information about the ARCHER solver, the reader can refer to e.g. [24, 38].

3.2. The oscillating droplet

The droplet at initial time corresponds to the prolate spheroid previously described in §2.3.3, i.e. with major axis a and minor axis b such as $a/b = 10/3$. We set $b = 50\ 10^{-6}$ m. The fluid physical properties are

as follows. The density is $\rho_L = 753$ kg.m^{-3} and $\rho_G = 25$ kg.m^{-3} for the liquid and gas phase, respectively. The dynamic viscosity is set to $\mu_L = 5.65\ 10^{-4}$ kg.m^{-1}.s^{-1}, $\mu_G = 1.879\ 10^{-5}$ kg.m^{-1}.s^{-1}. The surface tension $\gamma = 0.0135$ kg.s^{-2}. The computational domain is $L_x = L_y = L_z = 500\ 10^{-6}$ m and 384 grid points are used in all directions.

Thanks to the action of the surface tension forces, the droplet oscillates from prolate to oblate spheroid passing by a quasi-spherical shape. Figure 7 depicts the volume $V(d)$, surface area $S(d)$, mean curvature $H(d)$ and Euler characteristic $\chi(d)$ when the droplet is prolate ($t = 0$), quasi-oblate ($t = 0.78\tau_\gamma$) and quasi-spherical ($t = 1.23\tau_\gamma$). (In this figure the scale is normalized by $\mathcal{D} = 2b$ ($= 100$ μm).) For the three cases, the derivative $V(d)_{,d}$ is proportional to $S(d)$ (Fig. 7(b)) in agreement with Eq. (7)(a) and the Euler characteristic remains equal to 2 (Fig. 7(d)) since, whatever the scale, the eroded system remains homeomorphic to one sphere for the three cases displayed in this figure. However, these cases differ by the corrections introduced in Eqs. (7)(b) and (7)(c) to accurately represent the derivatives $S(d)_{,d}$ and $H(d)_{,d}$.

Identical to those plotted in Fig. 5, the curves for the prolate spheroid (case (1) in Fig. 7) evidence a correction $l_c C_2$ equal to zero and a correction C_3 well evaluated to accurately represent $H(d)_{,d}$. As explained above, C_3 increases from 0 to infinity when d varies from $0.3\mathcal{D}$ to $\mathcal{D}$ since the angle θ evolves from 0 to $\pi/2$.

The case (2) in Fig. 7 differs from the oblate spheroid by the presence of lugs at the poles. This difference explains why the curves of Figs. 6 and 7 (case (2)) are not the same although they are similar: both cases require corrections to recover $S(d)_{,d}$ and $H(d)_{,d}$. The medial axis of the quasi-oblate case is more complex than the one of the oblate spheroid. It has a circular basis (as for the oblate spheroid) with linear branches due to the lugs at the poles. Each element of this medial axis is meant to provide a contribution to the correction as resumed in Table I. The curves shown in Fig. 7 were established by considering the contribution of the circular medial axis only in the determination of the corrections $l_c C_2$ and C_3. As shown in Fig. 7, this does not degrade the capacity of the corrections to recover the derivatives $S(d)_{,d}$ and $H(d)_{,d}$, evidencing that the contribution to the correction of the medial axis linear element is negligible for this case.

Finally, case (3) in Fig. 7 corresponds to a quasi-spherical drop, the erosion of which produce no cusp whatever the scale. In this case, Eqs.(A.17) apply in agreement with the curves shown in Fig. 7.

The functions plotted in Fig. 7 provide a detailed description of the system and a huge amount of time and scale information offering numerous analysis possibilities that still need to be constructed. For instance, specific scales together with their temporal evolution can be identified. As an illustration, Fig. 8 displays the temporal evolution of two specific scales, $D_{\min}$ and $D_{\max}$, which are detected in Fig. 7 as follows. $D_{\min}$ is the largest scale for which the equality $2H(d)_{,d} = \chi(d)$ is satisfied. By definition, this scale is equal to twice the erosion-reach of the system. $D_{\max}$ is the smallest scale for which all functions plotted in Fig. 7 are equal to zero. The length $\mathcal{D}$ and the characteristic time $\tau_\gamma = (\rho_L \mathcal{D}^3/\gamma)^{1/2}$ ($= 0.236$ ms) normalize the scales and time, respectively.

During the oscillation mechanism, the droplet alternatively adopts a prolate and an oblate shape, which is respectively recognized by a linear and a circular medial axis. The prolate and oblate episodes are visualized as gray and white regions in Fig. 8, respectively. The driving surface tension forces responsible for the oscillation apply on the droplet poles during the prolate episodes whereas they apply on the whole equator circumference during the oblate episodes. This difference is important and explains the fact that the prolate episodes are longer ($\approx \tau_\gamma$) than the oblate ones ($\approx 0.6\tau_\gamma$). The period of the oscillation is therefore equal to $1.6\tau_\gamma = 0.378$ ms which is pretty close to the estimated value obtained from the theoretical expression given by [18] for small amplitude oscillation. Indeed, considering the first vibration mode, the oscillation period is estimated at 0.341 ms.

The green dot-line in Fig. 8 indicates the ratio $D_s/\mathcal{D}$ where D_s (≈ 150 μm) is the diameter of the droplet when it is spherical. Since the diameter of a sphere is equal to twice its erosion-reach as well as to its maximum scale, the droplet is spherical when $D_{\min} = D_{\max} = D_s$. During the oscillation sequence shown in Fig. 8, these equalities are never satisfied meaning that the droplet never hugs the spherical shape. This is when the shape changes from prolate to oblate, and vice versa, that the droplet is the closest to a sphere. The times corresponding to these situations are indicated by black vertical dash-dot lines in Fig. 8. At these times, the ratio $D_{\max}/\mathcal{D}$ exhibits a maximum that remains less than 1.5. On the other hand, the minima of $D_{\max}/\mathcal{D}$ occur at the times at which the droplet shape is furthest from the sphere. The level of these minima depends on the oscillation episode. During the prolate episodes, the minimum is reached when the droplet equator diameter is the smallest. Indeed, at these times, the scale $D_{\max}$ is equal to this specific diameter. During the oblate episodes, the minimum of $D_{\max}$ is reached when the distance between the droplet poles is the smallest, since $D_{\max}$ is equal to this very distance at these times. The maxima and minima of the scale $D_{\max}$ all increase from one oscillation period to the next one, evidencing an evolution of the system towards the stable spherical shape.

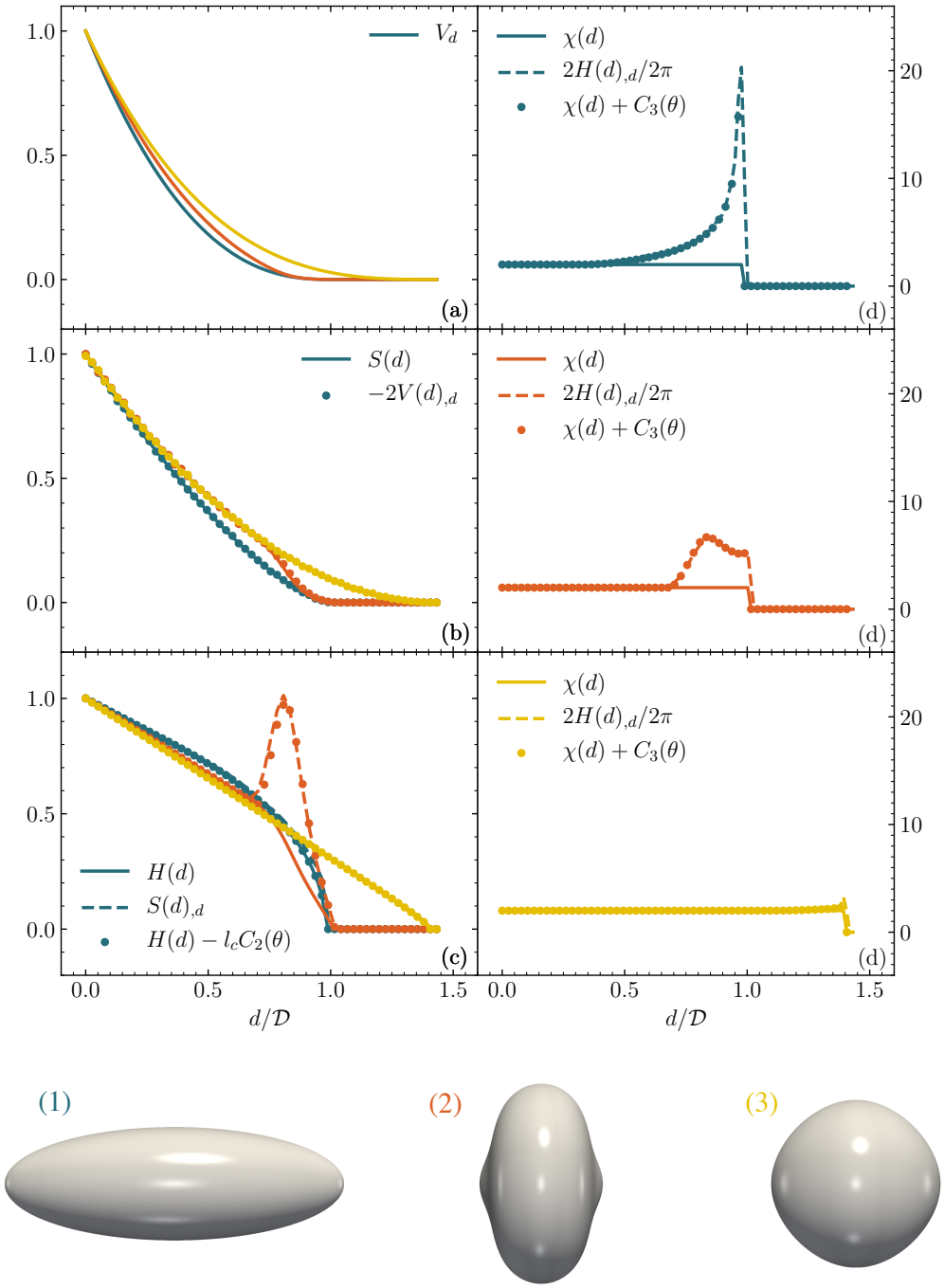

Figure 7: (a) Volume $V(d)$, (b) surface area $S(d)$, (c) mean curvature $H(d)$ and (d) Euler characteristic $\chi(d)$ as a function of the erosion scale d for the oscilating droplet. Results are for (1) $t = 0$, (2) $t = 0.78\tau_\gamma$ and (3) $t = 1.23\tau_\gamma$.

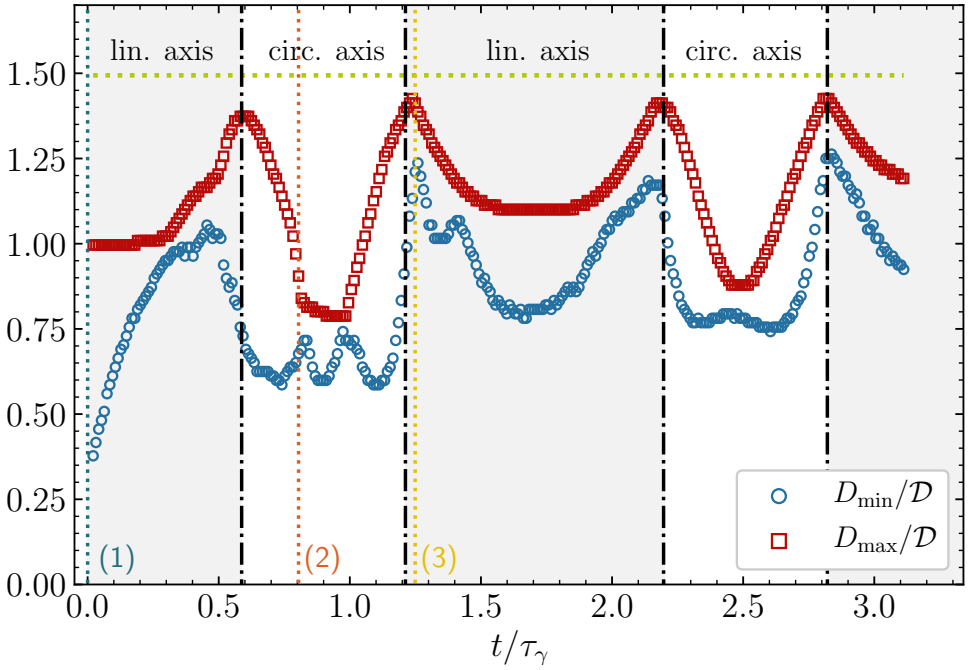

Figure 8: Time evolution of the reach $D_{\min}$ and maximum erosion scale $D_{\max}$ for the oscillating droplet. The vertical black lines depict the transition from oblate to prolate and the green horizontal line is the sphere equivalent diameter. The three time instant labelled (1) $t = 0$, (2) $t = 0.78\tau_\gamma$ and (3) $t = 1.23\tau_\gamma$ are also displayed by vertical dotted lines

The scale $D_{\min}$ provides further details on the shape of the drop during its oscillation. This scale may be representative of a mean curvature local extremum on the system interface (like in the extruded ellipse case) or of a local bottle neck (like in the extruded Cassini oval). In the first case, $D_{\min}$ is equal to twice the lower curvature radius, and, in the second, it is equal to the bottle neck size.

$D_{\min}$ and $D_{\max}$ display similar evolutions during the droplet oscillation: at each episode, they decrease, adopt a behaviour of less variation, and increase. At $t = 0$, the droplet is prolate and the scale $D_{\min}$ is imposed by the maximum curvature at the poles. During the early times, $D_{\min}$ increases while $D_{\max}$ remains constant. This shows that a modification of the shape of a specific region of the droplet needs time to deform farther regions of the system. Such a mechanism may be responsible for secondary deformations of the droplet during its oscillation. These secondary deformations are local and degrade the prolate or oblate configurations in a more or less pronounced way. The existence of secondary deformations is recognized in Fig. 8 by the time offset between the $D_{\min}$ and $D_{\max}$ signals and by specific $D_{\min}$ variations absent for $D_{\max}$. This is particularly observed during the two first episodes.

During the first episode, the relaxation of the initial prolate shape accumulates liquid in the poles that swell accordingly. As the relaxation continues, the swollen ends become preceded by a contracted region, mechanism that is accompanied by a change of slope in the increase of the scale $D_{\min}$ (at $t/\tau_\gamma \approx 0.25$). When the two contracted sections originating from each pole meet at the equator, the system resembles a peanut. This is its configuration at $t/\tau_\gamma \approx 0.45$ at which $D_{\min}$ displays a maximum that is equal to the diameter of the peanut equator. As relaxation continues, the contracted regions separate and continue their route toward the pole, opposite to the one they originate, where they disappear. At the same time, the global shape of the system passes from prolate to oblate due to accumulation of liquid in the equator region. The combination of these events makes the scale $D_{\min}$ decrease.

During the second episode, when the droplet is oblate, an oscillation of $D_{\min}$ appears at $0.6 < t/\tau_\gamma < 1.2$ while $D_{\max}$ remains roughly constant. This oscillation reflects a secondary deformation process. The first minimum of $D_{\min}$ corresponds to the presence of a remaining lug at the poles whose retraction in turn produces a flat interface (first maximum of $D_{\min}$), hollowed out (second minimum of $D_{\min}$), and then flat again (second maximum of $D_{\min}$). Finally, while the droplet begins its journey back to a prolate configuration, a lug reappears at the poles and $D_{\min}$ goes through the third and last minimum of this episode.

The evolution of $D_{\min}$ shown in Fig. 8 evidences that secondary deformation events are almost absent during the third and the fourth episodes: $D_{\min}$ appears more in phase with $D_{\max}$, approaches its value and

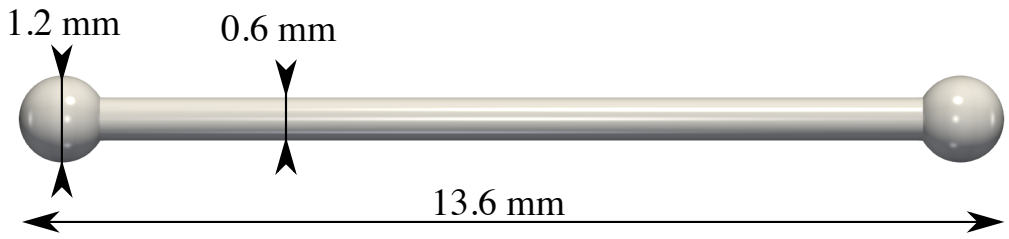

Figure 9: Initial condition for the retracting ligament simulation. This case corresponds to case (a) in Fig. 8 of Tong and Wang [35].

exhibits far less secondary variations. Such dynamic is representative of a stable system that rearranges as a sphere. In other words, the differences between the dynamics of $D_{\max}$ and $D_{\min}$, i.e., the primary and the secondary deformations respectively, should indicate whether the system is meant to divide or not during the oscillation process.

3.3. The relaxing ligament

Here, we consider the same case as Fig. 8(a) in Tong and Wang [35]. The initial geometry is that of an elongated cylindrical ligament closed with two spheres at each of its extremity, see Fig 9. The cylinder has an initial diameter 0.6 10^{-3} m and the droplets radius is 1.2 10^{-3} m. The ligament length is 13.6 10^{-3} m.

The liquid and gas density are $\rho_L = 1000$ kg.m^{-3} and $\rho_G = 1.2$ kg.m^{-3}, respectively. The viscosity of the liquid phase is $\mu_L = 1\ 10^{-3}$ kg.m^{-1}.s^{-1}, and that of the gas phase $\mu_G = 1.82\ 10^{-5}$ kg.m^{-1}.s^{-1}. The surface tension $\gamma = 0.073$ kg.s^{-2}. Only a quarter (half) of the ligament is simulated in the azimuthal (streamwize) direction. The computational domain is $L_x = 8L_y = 8L_z = 8\ 10^{-3}$ m and $1024 \times 128 \times 128$ grid points are used in x, y and z directions, respectively.

The relaxation of the elongated ligament caused by the action of surface tension forces deforms the system continuously inducing rupture and coalescence events. At $t = 1.43\tau_\gamma$, (where $\tau_\gamma = (\rho_L \mathcal{D}^3/\gamma)^{1/2} = 4.86$ ms) both spherical ends detach and form two oscillating spheres while the remaining ligament continues relaxing. At $t = 4.9\tau_\gamma$, the remaining ligament breaks up into three droplets with one tiny satellite between them. Moved by a velocity directed towards the center, the external drops coalesce with the satellites at $t = 5.19\tau_\gamma$ and with the central drop at $t = 5.75\tau_\gamma$. The simulation ends with three oscillating droplets, the one in the center being farther from the stable spherical shape than the two others.

The volume $V(d)$, surface area $S(d)$, mean curvature $H(d)$ and Euler characteristic $\chi(d)$ are plotted in Fig. 10 for the ligament at three different instants, i.e., $t = 0.57\tau_\gamma$ (before the first breakup event), $t = 3.59\tau_\gamma$ (between the two breakup events) and $t = 5.84\tau_\gamma$ (after the second coalescence event). As for the previous case and in agreement with Eq. (7)(a), the surface area $S(d)$ appears proportional to the derivative $V(d)_{,d}$ irrespective of the scale for the three cases (Fig. 10(b)). Furthermore, since the ligament shows a linear medial axis at each time during the relaxation mechanism, the mean curvature $H(d)$ requires no correction to reproduce the derivatives $S(d)_{,d}$ (Fig. 10(c)) in agreement with the element listed in Table 1.

Contrary to the previous case that reported a constant Euler characteristic (see Fig. 7), $\chi(d)$ depends on the scale as shown in Fig 10(d) for cases (1), (2) and (3), respectively. As observed for the extruded Cassini oval (Fig. 4), this scale dependence reveals that the eroded systems may be constituted of disconnected elements the number of which being a function of the erosion scale. As shown in Fig. 10, the ligament rearranges as a succession of contracted or bottle neck sections separated by swelled sections. Performing an erosion at a scale equal to a bottle neck diameter produces an eroded system made of disconnected elements whose number imposes the increase of the Euler characteristic. On the other hand, performing an erosion at a scale equal to a swelled section diameter erases the contribution of this swell to the eroded system, decreasing the Euler characteristic accordingly. Therefore, the scales for which $\chi(d)$ jumps up are bottle neck diameters, the number of these bottle necks being given by the height of $\chi(d)$ jump. The scales for which $\chi(d)$ jumps down are swell diameters, the number of these swells being given by the height of $\chi(d)$ jump. This shows to which extend $\chi(d)$ provides quantitative information on the system morphology.

As observed for the extruded Cassini oval, the derivative $H(d)_{,d}$ shows a peak at each Euler characteristic jump. Since the peak shape depends on whether $\chi(d)$ jumps up or down, information on the number and scale of the bottle necks and swells are also available from $H(d)_{,d}$. Once again, Figs. 10(d) shows that Eq. (7)(c) together with the elements of Table 1 allow a correct representation of the function $H(d)_{,d}$.

As done for the oscillating droplet in the previous subsections, Fig. 11 shows the temporal evolution of the specific scales $D_{\min}$ and $D_{\max}$. The positions of cases (1) to (3) are indicated by the dot lines and the

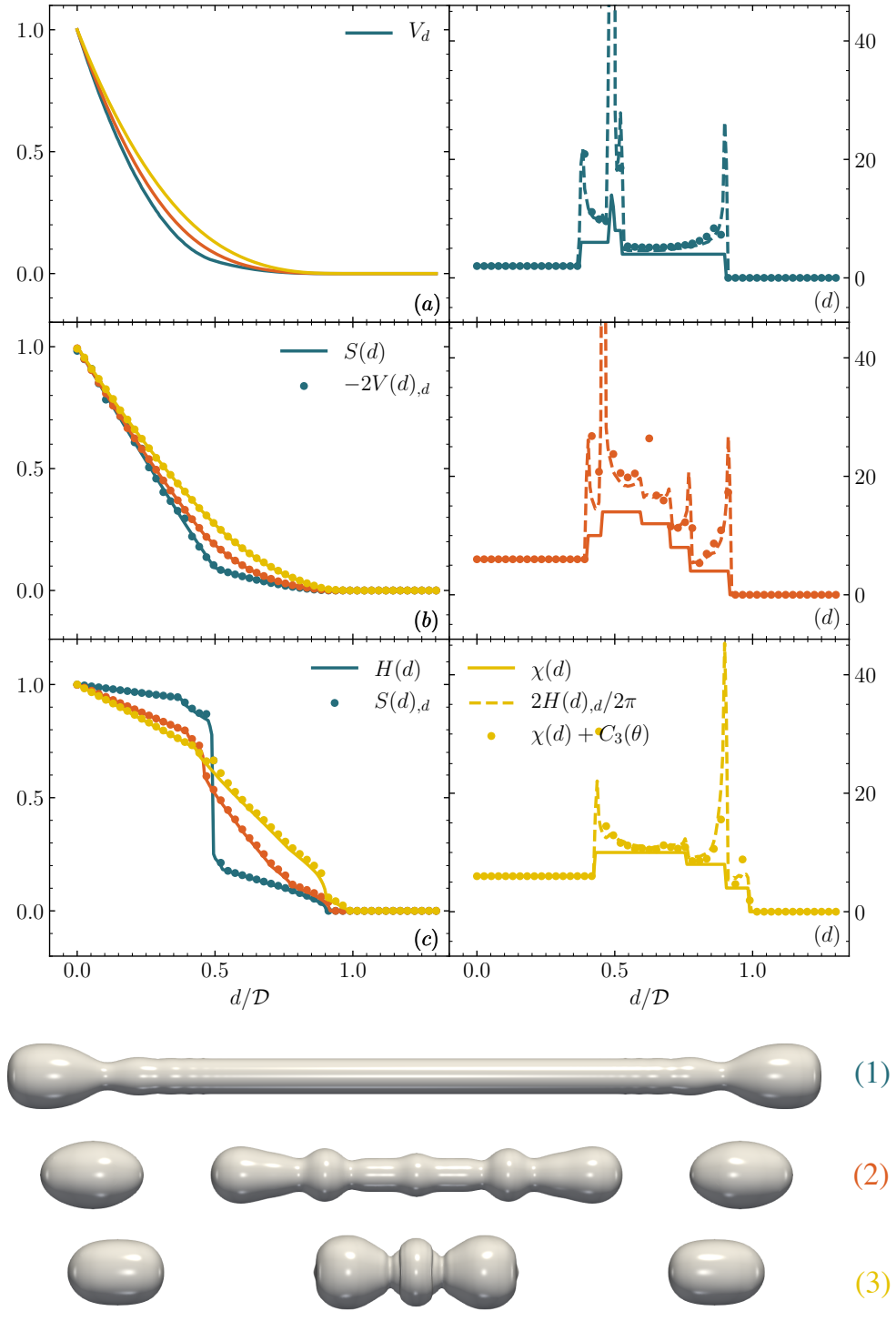

Figure 10: (a) Volume $V(d)$, (b) surface area $S(d)$, (c) mean curvature $H(d)$ and (d) Euler characteristic $\chi(d)$ as a function of the erosion scale d for the retracting ligament. Results are for $t/\tau_\gamma =$ (1) 0.57, (2) 3.59, (3) 5.84.

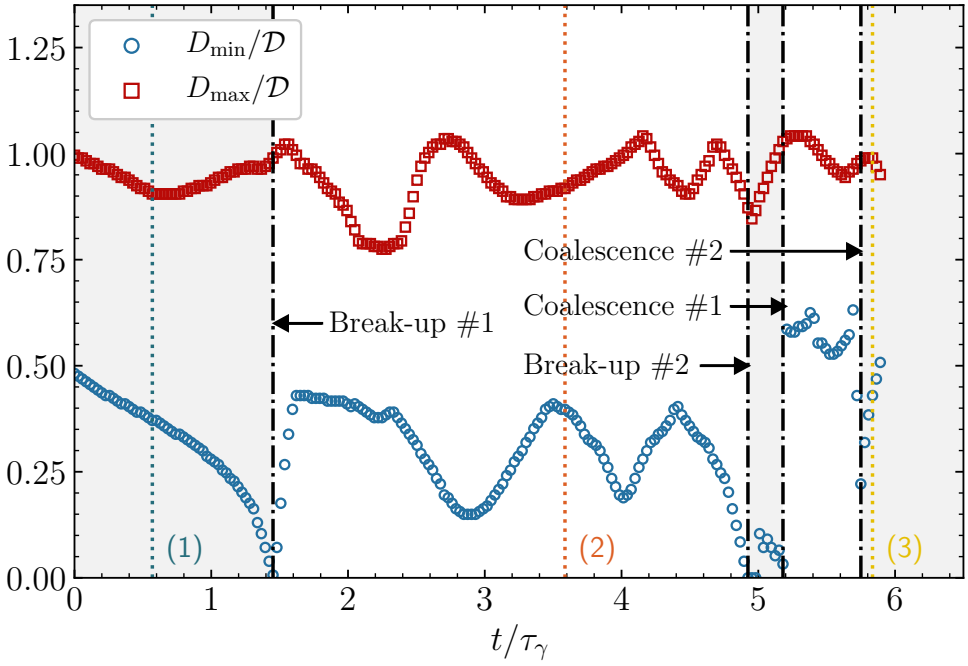

Figure 11: Time evolution of the reach $D_{\min}$ and maximum erosion scale $D_{\max}$ for the retracting ligament. The vertical black lines depict either break-up or coalescence events. The three time instant $t/\tau_\gamma =$ (1) 0.57, (2) 3.59, (3) 5.84 are also displayed by vertical dotted lines

break-up and coalescence events by the black dot-dash lines.

Between $t/\tau_\gamma = 0$ and 3.6, D_{max} is carried by both system ends that become independent oscillating drops after the first break-up event at $t/\tau_\gamma = 1.45$. Initially spherical, these ends oscillate from quasi-prolate to quasi-oblate spheroids reporting a $D_{\max}$ evolution similar to the one obtained for the oscillating droplet (Fig. 8). For time higher than $t/\tau_\gamma = 3.6$, D_{max} is carried by either elements of the system, explaining the oscillation of this scale between $t/\tau_\gamma = 4$ and 5.

We see in Fig. 10 that the scale $D_{\min}$ corresponds to the first peak of $H(d)_{,d}$ indicating that this scale is always equal to a bottle neck or pinch-off diameter. Before the first break-up event, $D_{\min}$ is the diameter of the pinch-off ensuring the contact of the ends to the ligament. It decreases continuously and reaches zero at the time of the first break-up.

Between the two break-up events, D_{min} is carried by the remaining ligament between the external drops. This scale oscillates, following the evolution of the smallest ligament pinch-off. The satellites between the three drops produced by the second break-up impose the small D_{min} after $t/\tau_\gamma = 4.95$, and their disappearance by the first coalescence event is recognized by the sudden increase of D_{min} at $t/\tau_\gamma = 5.2$. Finally, the coalescence of the three central droplets (at $t/\tau_\gamma = 5.75$) produces contact pinch-offs between the drops and D_{min} becomes equal to the diameter of these pinch-offs explaining its small value found at this time. The vivid increase of D_{min} after this event augurs well for the evolution of the central element towards a spherical shape.

3.4. The Plateau-Rayleigh instability

This section presents the case of a cylindrical ligament subject to the surface tension driven Rayleigh-Plateau instability. We employ the same numerical configuration as [5]. The liquid and gas density are $\rho_L = 1000$ kg.m^{-3} and $\rho_G = 1$ kg.m^{-3}, respectively. The viscosity of the liquid phase is $\mu_L = 1\ 10^{-3}$ kg.m^{-1}.s^{-1}, and that of the gas phase $\mu_G = 1.879\ 10^{-5}$ kg.m^{-1}.s^{-1}. The surface tension $\gamma = 0.072$ kg.s^{-2}. The ligament has an initial radius $a = \overline{k}L_x/\pi$ where the non-dimensional perturbation wavenumber $\overline{k} = ka = 0.55$ applies on the x axis. The amplitude of the perturbation was set to $0.1a$. Only a quarter (half) of the ligament is simulated in the azimuthal (streamwize) direction. The computational domain is $L_x = 3L_y/2 = 3L_z/2 = 1.5\ 10^{-4}$ m and $192 \times 128 \times 128$ grid points are used in x, y and z directions, respectively.

For the selected sinusoidal perturbation wave-number, the cylindrical ligament is unstable and, according to the Rayleigh theory, the perturbation temporal growth rate is equal to $\omega = 0.318\tau_\gamma/(8)^{1/2}$ (where $\tau_\gamma =$

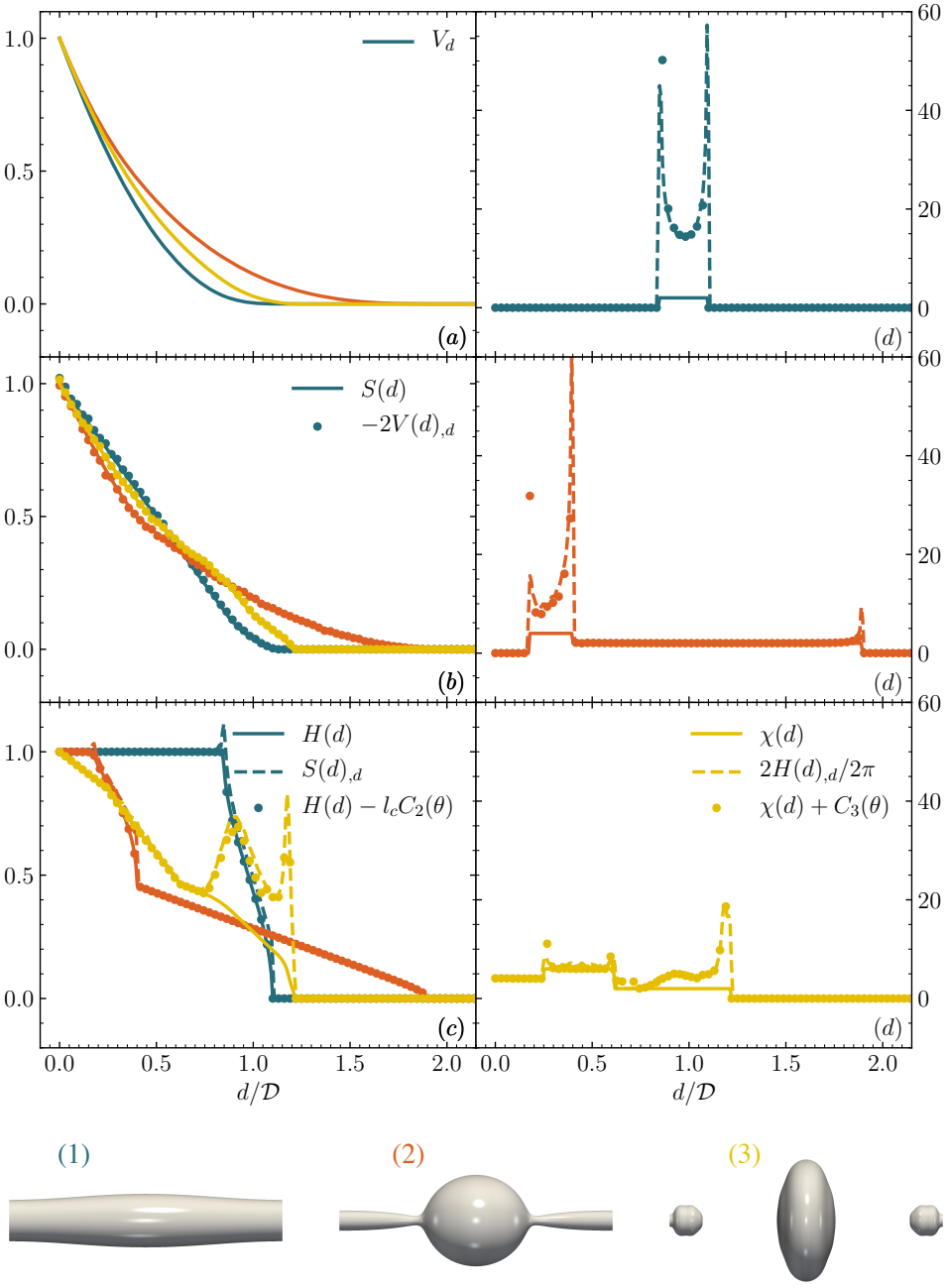

Figure 12: (a) Volume $V(d)$, (b) surface area $S(d)$, (c) mean curvature $H(d)$ and (d) Euler characteristic $\chi(d)$ as a function of the erosion scale d for a liquid ligament undergoing the Plateau-Rayleigh instability. Results are for t/τ_{bu} = (1) 0.42, (2) 0.96, (3) 1.09.

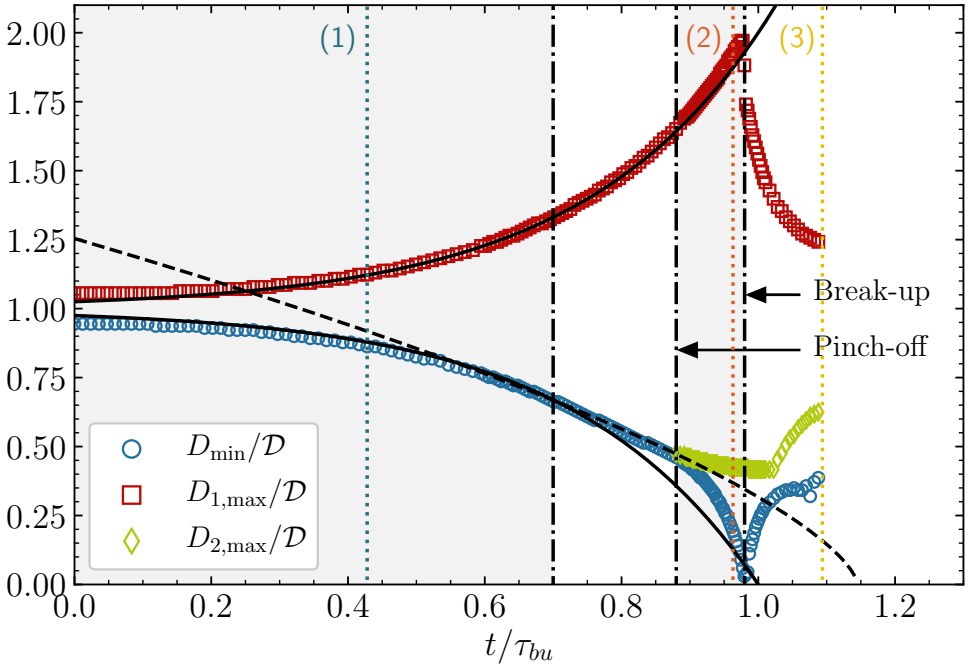

Figure 13: Time evolution of the reach $D_{\min}$, the maximum erosion scale $D_{1,\max}$ and the size of the satelite maximum erosion scale $D_{2,\max}$ for the Plateau-Rayleigh instability. The two vertical black lines depict the first departure of $D_{\min}$ from an exponential behavior and the apparition of the pinch-off, respectively. The three time instant labelled (1) $t = 0.42\tau_{bu}$, (2) $t = 0.96\tau_{bu}$ and (3) $t = 1.09\tau_{bu}$ are also displayed by vertical dotted lines

0.045 ms) and the break-up time is $t_{bu} = \tau_\gamma log(D/2\eta_0)/(\omega(8^{1/2}))$, i.e., $\tau_{bu} = 0.115ms$. The deformation of the ligament manifests first by a growth of the amplitude of the sinusoidal perturbation and, second, by a rearrangement of the ligament as an almost spherical bead connected with a small scale ligament. The rupture of this structure produces one big drop (from the bead) and one satellite drop, the latter coming from the relaxation of the small ligament when left alone after the break-up.

Figure 12 presents the functions $V(d)$, $S(d)$, $H(d)$ and $\chi(d)$ for the three cases, i.e., during the initial sinusoidal perturbation growing (case (1)), just before the break-up event (case (2)) and after the break-up event (case (3)). As for the previous situations, we note that the functions $S(d)$ and $V(d)_{,d}$ remain proportional with each other for the three cases (Fig. 12(b)). As expected from the prolate spheroid (Fig. 5) or the relaxing ligament (Fig. 10), the functions $H(d)$ and $S(d)_{,d}$ match well for cases (1) and (2), i.e., those having a linear medial axis and requiring no correction at this level. Since case (3) shows an quasi-oblate element, a correction of $H(d)$ appears necessary to retrieve $S(d)_{,d}$. Once again we note that the correction provided by Eq. (7) apply very well. Although the main drop of case (3) is quasi-oblate, note that the function $S(d)_{,d}$ is rather different than the one obtained in Fig. 6 for the exact oblate spheroid or the one in Fig. 7 when the oscillating droplet is almost oblate. These observations underline the sensitiveness of the functions displayed in these figures.

Since the system remains homeomorphic to a cylinder before break-up, the Euler characteristic $\chi(0)$ is equal to zero for cases (1) and (2) (see Fig. 12(d)). However, for other scales, $\chi(d)$ varies according to the number of elements that constitute the eroded system. As described in the previous section, this number increases when the erosion scale matches the diameter of a bottle neck or a pinch-off, or decreases when the erosion scale matches the diameter of a swell section. The scales concerned by this Euler characteristic change are rendered visible by the peaks of the function $H(d)_{,d}$. (Note that, here again, Eq. (7) and the elements of Table 1 combine very well and ensure a good representation of the function $H(d)_{,d}$). For case (1), the first peak indicates the scale of a bottle neck and the second one the one of a swell. These scales correspond to the smaller and larger diameters of the deformed ligament, respectively. For case (2), the first peak indicates the diameter of the pinch-off between the ligament and the bead, the second peak indicates the larger diameter of the ligament and the third peak is the characteristic scale of the bead. For case (3) $\chi(0) = 4$ since the system has transformed as two drops. This value changes as a function of the scale indicating that these drops are not fully spherical yet.

Figure 13 displays the temporal evolution of three specific scales: $D_{\min}$, $D_{1,\max}$ and $D_{2,\max}$. (The time

is normalized by the theoretical break-up time τ_{bu}.) These scales are those at which $H(d)_{,d}$ exhibits a peak. Since the reach of the system, i.e. the scale $D_{\min}$, is associated with a peak of the function $H(d)_{,d}$, it always corresponds to the radius of a bottle neck or of a pinch-off.

The unstable nature of this system is manifested by a marked divergence of the scales $D_{\min}$ and $D_{1,\max}$. The scale $D_{1\,\max}$ continuously increases following very well the exponential growth obtained from the linear theory and shown by the black line. Similarly, the scale $D_{\min}$ reports a continuous decrease that follows the theoretical behavior up to $t/\tau_{bu} = 0.7$. After this time, the linear theory is not appropriate anymore to reproduce the evolution of $D_{\min}$ which, therefore, is likely affected by the first action of non-linear effects. The black dash line in Fig. 13 shows that $D_{\min}$ decreases as $t^{2/3}$. As reported by the literature [e.g. 10] this temporal dependence reveals that the pinch-off contraction has reached an inertial regime for which the dominant resistance against surface tension stems from the inertia of accelerating fluid elements. This regime lasts until $t/\tau_{bu} = 0.9$ after which another dynamics appears. This last behavior likely represents the visco-capillary regime for which the dominant resistance against surface tension stems from viscous forces. The theory predicts a linear dependence between the pinch-off diameter and the time for this regime that is not obvious in Fig. 13 although the points seem to align close to the break-up event. At this very time ($t/\tau_{bu} = 0.9$), a third peak of $H(d)_{,d}$ appears at scale $D_{2,\max}$. The appearance of this scale demonstrates that the pinch-off evolution divides the liquid system in two isolated parts, confirming the approach of a break-up event. Each of these parts have their own maximum scale, $D_{2,\max}$ being the one of the ligament. We see that during break-up, this scale does not vary significantly.

The multi-scale analysis is validated here by the fact that it allows us to find the known behaviors of D_{min} and D_{max}. Note that it offers an alternative to the problems posed by traditional approaches, which require the localization of scales before their measurement, a step that proves to be a source of imprecision. The multi-scale approach involves only one measurement, that of a function which, beyond the scales D_{min} and D_{max} presented here, contains a significant amount of information.

3.5. The two-phase homogeneous isotropic turbulence

The present framework is now applied to appraise the morphology of liquid structures in a turbulent flow. For this purpose, we use the same flow configuration as the one explored by [5, 12, 32, 34], i.e. a two-phase flow evolving in a triply periodic turbulent flow. The square box is filled with 5% of liquid and the four initially spherical liquid structures get contorted through the action of turbulence. The latter is linearly forced so that the turbulent kinetic energy remains constant and equal to 3.6 $\mathrm{m}^2.\mathrm{s}^{-2}$. We use the same physical parameter as [32, 34]. The density of liquid and gas phases are set to $\rho_L = 753$ $\mathrm{kg.m}^{-3}$ and $\rho_G = 25$ $\mathrm{kg.m}^{-3}$, respectively, leading to a density ratio of about 30. The dynamic viscosity for the liquid and gas phase are $\mu_L = 5.65\ 10^{-4}$ Pa.s and $\mu_G = 1.879\ 10^{-5}$ Pa.s, respectively. Therefore, the kinematic viscosity is the same for both the liquid and gas phase. Compared to [32, 34], we used a slightly higher surface tension $\gamma = 0.0189$ $\mathrm{N.m}^{-1}$ which was proven to enhance the number of generated liquid structures. The domain is discretized using 256 points in all three directions. The domain is square and $1.5\ 10^{-4}$ m wide in each direction. These parameters lead to a turbulent Reynolds number based on the kinetic energy and integral length scale of 194, the Taylor microscale Reynolds number is 25, the turbulent Weber number is 5.8. The ratio of the Taylor microscale and Kolmogorov length scale to the mesh cell size is 20.0 and 2.05 respectively.

We have selected three typical structures which are colored in blue, red and yellow in Fig. 14. Note that although the yellow structure appears disconnected, the surfaces on top and bottom of the domain belongs to the same structure because of periodicity. We have computed their corresponding MFs which are plotted in Fig. 15. The erosion scale d is normalized by the sphere equivalent diameter noted $D_{eq,s} = (3V(d = 0)/4\pi)^{1/3}$. $V(d), S(d)$ and $H(d)$ are normalized by the sphere equivalent volume $(\pi D_{eq,s}^3/6)$, surface $(\pi D_{eq,s}^2)$ and mean curvature $(2\pi D_{eq,s})$, respectively. We note that for all three structures, $S(d) = -2V(d)_{,d}$ meaning that this result is rather general and holds even for more complicated morphology than the ones previously analysed. Looking at the Euler characteristic in Fig. 15, we note that $\chi(d = 0) = 2$ meaning that all three structures are homomorphic to a sphere. The blue curve in Fig. 15 indicates that the corrections C_2 and C_3 which are given by $H(d) - S(d)_{,d}$ and $\chi(d) - H(d)_{,d}/\pi$, respectively, are almost zero for almost all values of the morphological parameter d. This means that the structure under consideration is roughly spherical which is indeed observed in Fig. 14. For this structure, we have $S(d = 0)$ and $H(d = 0)$ which are almost equal to their sphere equivalent value. The red curve reveals that the correction C_2 is almost zero while C_3 reveals two distinct peaks with significant values. Given our previous analysis of the Plateau-Rayleigh instability, we can conclude that such distributions of C_2 and C_3 are representative of an elongated structure, i.e. characterized by a quasi linear medial axis. The peak at the smallest d can be associated to the presence of a pinch-off

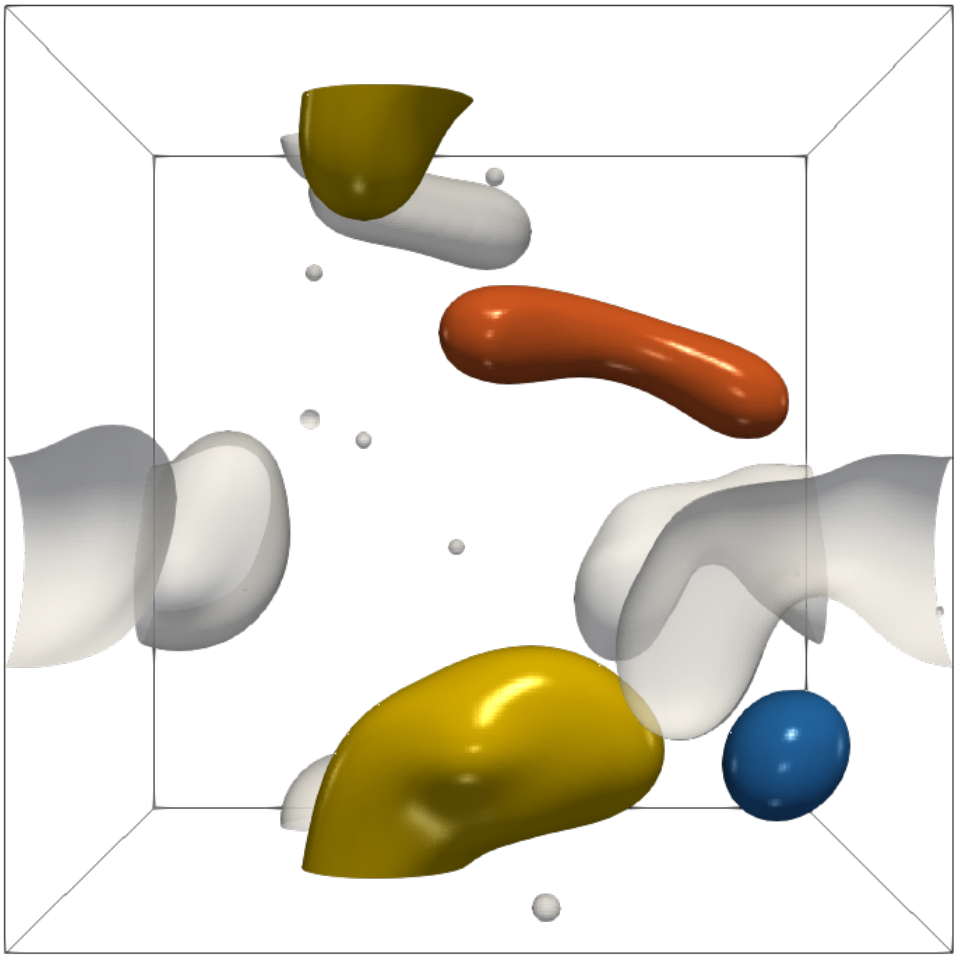

Figure 14: Direct visualization of three structures (represented in blue, red and yellow) evolving in a liquid-gas homogeneous isotropic turbulence

with size $\approx 0.45 D_{eq,s}$. The second peak is representative of a bulge whose size is about $0.55 D_{eq,s}$. This is consistent with the direct visualization of the red structure given in Fig. 14. Finally, the yellow structure which appears much more contorted than the two others is characterized by non zero corrections for both $H(d)$ and $\chi(d)$. C_2 and C_3 start being non zero for scales larger than $0.25 D_{eq,s}$ which provides a measure of the reach of the system under consideration. The scale dependence of C_2 for scales d larger than $0.25 D_{eq,s}$ indicates that the yellow structure might be rather flat, i.e. with a medial axis falling along a surface. This is indeed observed in the actual visualization of this structure given in Fig. 14.

We see again on this application that the description of parallel systems by the MFs brings more information than the only description of the system at the erosion scale $d = 0$. As we have done here, MFs can be computed for all individual structures. Since they are additive, the morphology of the total system can simply be deduced from the sum of the MFs of individual structures. In what follows, we perform such kind of analysis.

3.6. Ligament mediated atomization.

The last example of the present framework application concerns a ligament mediated atomization process. Contrary to the previous examples, the application is made here on experimental results (the details of the experiment are available in [39]). The atomizer is equipped with a triple-disk nozzle known to favor the development of a turbulent flow with a double contra-rotating swirl which results in the production of a

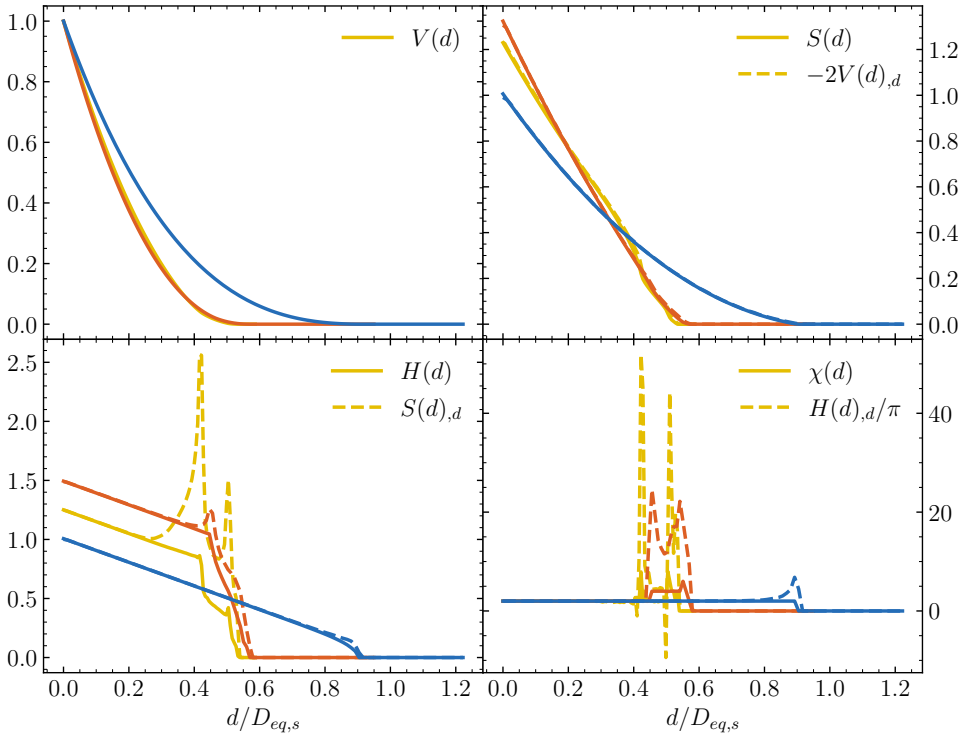

Figure 15: MFs of three typical structures evolving in a liquid-gas homogeneous isotropic turbulence.

2D highly-perturbed liquid sheet. Turbulence is a source of disturbances, some of which, selected by the action of surface tension forces, deform the edges of the sheet in a rather regular and reproducible way and structure its contraction into a network of deformed lateral ligaments, the rupture of which produces drops of different sizes. Fig. 16 is a snapshot of the process in the region extending from about 10 to 28 nozzle diameters denoted D_i ($D_i = 400$ μm, see [39]), region where the drop production is the more effective. We see the end of the contraction of the liquid sheet and its reorganization into lateral ligaments as well as the break-up of these ligaments into drops. This atomization process is mainly 2D and what is observed in Fig. 16 is representative of the whole flow evolution.

The MFs of the liquid system are measured on images similar to the one in Fig. 16 after appropriate image processing [4]. In order to compute the MFs using the exact same numerical tools as the one used heretofore, the liquid observed in the 2D image is simply extruded over the third direction. A fictitious constant thickness $h = 1$, is used. Thus, the MF $V(d)$ is equal to the liquid surface projected area (times $h = 1$), $S(d)$ is equal to the liquid system perimeter (times $h = 1$) and $H(d)$ is equal to the length averaged mean curvature. The fourth MF related to the Gaussian curvature is equal to zero since the curvature in the extruded direction is zero. Note that in this two-dimensional description, the length-averaged mean curvature $H(d)$ carries the role of the Euler characteristic $\chi(d)$, i.e., $H(d) = -\pi\chi(d)$. Since the flow is inhomogeneous, the MFs are measured on five distinct portions of the liquid system delimited by the colored rectangles shown in Fig.16. The measurements are performed on 150 images and the averaged MFs are displayed in Fig.17 where the curve colors indicate the measurement locations and where D_i is the nozzle orifice diameter.

The top graph in Fig.17 presents the volume $V(d)$. As expected, this function decreases with the scale d, and, for all scales, $V(d)$ continuously decreases with the distance from the injection point. This latter behavior reflects the decrease of the projected surface area as the liquid sheet contracts and reorganizes as ligaments. The sheet contraction is also evidenced by the decay of the larger scale as one moves away from the injector.

The middle graph in Fig.17 displays the measured $S(d)$ and the derivative $-2V(d)_{,d}$. As for all cases examined in the previous sections of this paper, the equality $S(d) = -2V(d)_{,d}$ still applies at all scales. At large scales, i.e., those representative of the sheet, $S(d)$ is much smaller than at small scales and continuously decreases with the downstream position. This illustrates the small interface length carried by the sheet as well as its disappearance while reorganizing as ligaments. At small scales, $S(d)$ increases continuously for all

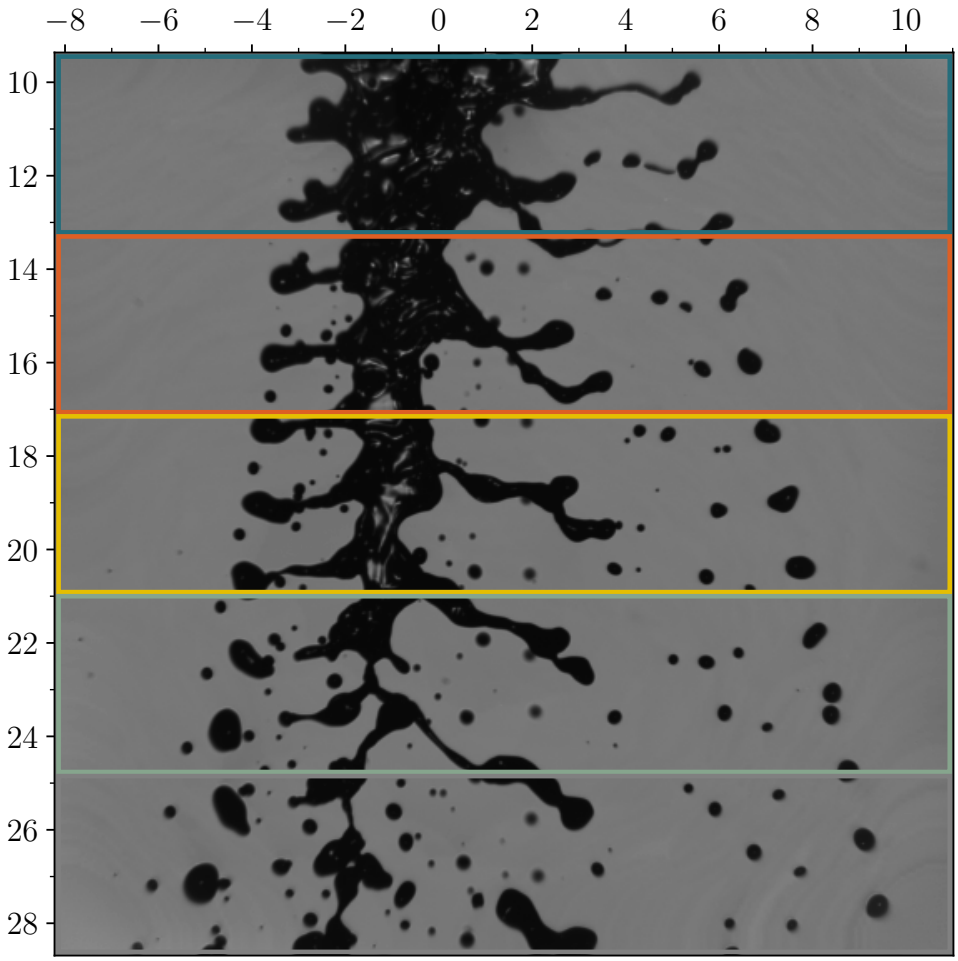

Figure 16: Triple-disk atomizer liquid sheet atomization process; Orifice diameter $D_i = 400\mu$m; water + 10% isopropanol, liquid sheet velocity: 9.14 m/s; The streamwise and transverse coordinate axis are given in units of D_i; Refer to Vu and Dumouchel [39] for further detail.

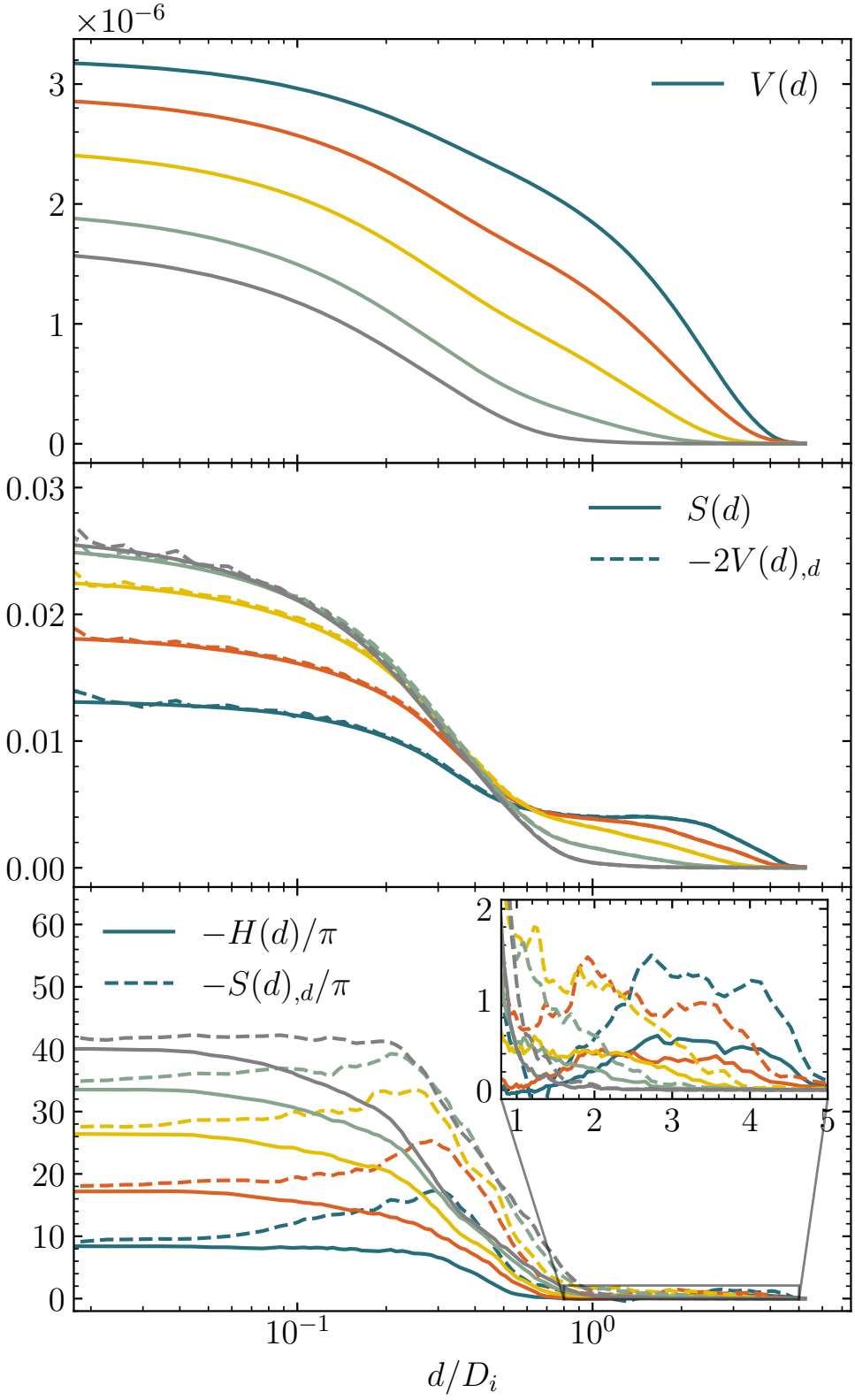

Figure 17: MFs of the liquid system shown in Fig. 16 according to position (matching those in Fig. 16 the colors indicate the position) Top graph: Volume $V(d)$ (m^3); Middle graph: Surface $S(d)$ and derivatives $-2V(d)_{,d}$ (m^2); Bottom graph: $-H(d)/\pi$ and the derivative $-S(d)_{,d}/\pi$ (m)

scales as a function of the downstream position. This behavior underlines the increase of interface associated with the development and atomization of the ligaments. It is interesting to note that the interface quantity represented by $S(d)$ appears to converge to its equilibrium value whilst the breaking process is not yet complete.

The bottom graph in Fig.17 displays the measured mean curvature $-H(d)/\pi$ and the derivative $-S(d)_{,d}/\pi$. Being the average of 150 measures, $-H(d)/\pi$ is not limited to integer values only and displays a smooth continuous behavior. Its value for $d = 0$ ($-H(0)/\pi$) corresponds to the average number of disjoint elements: the drop production process makes this number increase with the position. $-H(d)/\pi$ and $-S(d)_{,d}/\pi$ are not equal due to the complex shape of the liquid structures. While $-H(d)/\pi$ represents the average number of disjoint liquid elements, $S(d)_{,d}/\pi$ additionally carries information about their characteristic scales. Thus, in the region of large scales (see the insert on the figure) $S(d)_{,d}/\pi$ shows two main peaks at two characteristic scales, i.e., the average smallest and largest widths of the sheet. We see that these scales decrease with the downstream position. This is representative of the rate at which the sheet contracts, which can thus be measured here.

In the small scale region, $-H(d)/\pi$ and $-S(d)_{,d}/\pi$ separate at a scale corresponding to the averaged reach of the liquid system. The absence of a peak of $-S(d)_{,d}/\pi$ at this scale indicates that the reach corresponds to the smallest curvature radius as for the case of the extruded ellipse (Fig. 3) and not to the pinch-off size as for the case of the extruded Cassini oval (Fig. 4). The decrease of the averaged reach with the downstream position illustrates the presence of smaller and smaller drops. When the scale d exceeds the reach, $-H(d)/\pi$ begins to decrease, indicating the loss of small drops. This coincidence shows that the reach well corresponds to the radius of the small drops. At the same time, $-S(d)_{,d}/\pi$ increases until it reaches a maximum and then decreases continuously to 0. The scale at which $-S(d)_{,d}/\pi$ is maximum decreases with the downstream position. The behavior of $-S(d)_{,d}/\pi$ with the scale d integrates two mechanisms: the decrease of the number of disjoint elements (topological information) and the increase of the $C_2(\theta)$ correction with the erosion scale for the remaining elements (morphological information). When $-S(d)_{,d}/\pi$ increases, the second mechanism prevails over the first; when it decreases, it is the opposite. When $-S(d)/\pi$ is constant, the two mechanisms annihilate (see last position results in Fig. 17). Thus, the decay of $-S(d)_{,d}/\pi$ after the maximum is representative of the maximum scale distribution of main structures. Note that when $-S(d)_{,d}/\pi$ starts decaying, $-H(d)/\pi$ starts decreasing more quickly. The end of the atomization process (all drops are spherical) will be characterized by the equality $-S(d)/\pi = -H(d)/\pi$ and this unique function can be shown to be directly proportional to $(1 - F_0(D))$ where $F_0(D)$ is the cumulative number-based drop-diameter distribution ([33]). The decays of the functions shown in Fig.17 will therefore converge to the drop diameter distribution which must undoubtedly lie between the functions $-H(d)/\pi$ and $-S(d)_{,d}/\pi$.

This last application illustrates the richness of MFs for the description of atomization processes with the possibility to identify characteristic scales of the structures involved and to study their dynamics. We demonstrate here the possibility of using this approach on images provided by the experiment offering access to many quantitative information to describe and study an atomization process.

4. Conclusion

The present work is motivated by the need of liquid morphological descriptors that aim at supplementing the drop size distribution which is inoperative for describing the primary atomization zone. The conclusions of the present analysis concern both the mathematical development and its application.

From a mathematical point of view, the links between Minkowski Functionals for systems parallel to an initial system have been established for all possible distances. If these relationships had already been established for distances below the initial system reach, this was not the case for distances beyond this reach. This result is obtained using tools from integral geometry. The reader is advised to refer to Appendix A.3 and Appendix B for technical details. It is worth stressing that the analysis is carried for simple bodies (extruded and axisymmetric shapes) which has allowed us to extract the following key features. While the relationships between the MFs of parallel surfaces only involve their successive derivatives when the distance remains less than the reach, they depend, for scales beyond the reach, on the shape of the medial axis and on local properties of the interface such as the angle between the normal of the parallel surface at the cusps and the initial system medial axis. The dependence of the MFs with the interface local property allows identifying specific scales such as those for which a bottle-neck or a bulge appears. This analysis suggests that a complete morphological description of complex shapes requires the weighted medial axis (where the distance of the interface is known for each medial axis point) to be supplemented by an information about the angle between the cusp normal and the medial axis.

As far as the application of such analysis to free liquid systems is concerned, the first result is an indication on the equilibrium of any structure: indeed, a liquid structure with a reach less than the maximum scale reveals the existence of a deformation dynamic. Furthermore, the ability of the analysis to identify the bottlenecks is of great use in studying their dynamics and their possible evolution towards a pinch-off and a breakup event. Applied to the Rayleigh-Plateau instability, this paper demonstrates that the analysis is suited for probing the dynamics of the large scale and of the pinch-off mechanisms. In this analysis, the reach of the system (scale D_{min}) appears to be a very important indicator. In addition to the identification and following over time of bottlenecks, this scale provides information on the presence of local deformations, named secondary deformations, when they involve small scales that cause a decrease of the reach. These deformations are important because they can, in some cases, trigger local rupture processes. Such situations have not been investigated for the moment.

Finally, this work demonstrates the possibility of using MFs to describe and quantify experimental observations. Even if the information is 2D, the description of the series of parallel systems produces comprehensive quantitative informations whose evolution in space or time is accessible. These evolutions are new elements for the study of atomization processes.

In conclusion, the MFs are nicely tailored for inferring the morphology of the structures under consideration. They provide a qualitative assessment of their shape (spherical, elongated, flat) together with a quantitative measure of their characteristic scales (reach, pinch-off and bulges size). They thus contain a much richer information than the one exclusively contained at $d = 0$ or the one deduced from their sphere equivalent value. The two-point structure function of the phase indicator [32–34] and the following over time of the MF of parallel systems constitute relevant multi-scale analysis tools for the study of dynamic heterogeneous systems. Contrary to the phase indicator statistics, the MF at different erosion scales lack of a transport equation. Nevertheless, it can be used as a support to develop models as, for example, illustrated by a previous work devoted to the representation of an atomization process by the scale entropy diffusion model [11].

Declaration of Competing Interest

The authors declare that they have no known competing financial interests or personal relationships that could have appeared to influence the research reported in this paper.

Acknowledgements

Computations have been carried out in CRIANN (Centre Rgional Informatique et dApplications Numriques de Normandie) under the project 2018002. FT also benefited from the financial support from the INSIS institute of the CNRS and the CORIA laboratory which are gratefully acknowledged. We are also grateful to M. Massot for sharing the routines allowing us to compute the surface area and curvatures of iso-level-set surfaces. These are now available through the project Mercur(v)e (http://docs.mercurve.rdb.is/).

References

[1] PM Adler, Ch G Jacquin, and JA Quiblier. Flow in simulated porous media. *Int. J. Multiphase Flow*, 16(4):691–712, 1990.

[2] Christoph H Arns, Mark A Knackstedt, and Klaus R Mecke. Characterisation of irregular spatial structures by parallel sets and integral geometric measures. *Colloids and Surfaces A: Physicochemical and Engineering Aspects*, 241(1-3):351–372, 2004.

[3] James G Berryman. Relationship between specific surface area and spatial correlation functions for anisotropic porous media. *J Math Phys*, 28(1):244–245, 1987.

[4] JB Blaisot and J Yon. Droplet size and morphology characterization for dense sprays by image processing: application to the diesel spray. *Experiments in fluids*, 39(6):977–994, 2005.

[5] R Canu, S Puggelli, M Essadki, B Duret, T Menard, M Massot, J Reveillon, and FX Demoulin. Where does the droplet size distribution come from? *Int. J. Multiphase Flow*, 107:230–245, 2018.

[6] S Ciccariello. Integral expressions of the derivatives of the small-angle scattering correlation function. *J. Math. Phys.*, 36(1):219–246, 1995.

[7] P Debye, HR Anderson Jr, and H Brumberger. Scattering by an inhomogeneous solid. ii. the correlation function and its application. *J Appl Phys*, 28(6):679–683, 1957.

[8] R Di Battista, I Bermejo-Moreno, T Ménard, S de Chaisemartin, and M Massot. Post-processing of two-phase dns simulations exploiting geometrical features and topological invariants to extract flow statistics: application to canonical objects and the collision of two droplets. In *10*$^{\text{th}}$ *International Conference on Multiphase Flow, Rio de Janeiro, Brazil*, 2019.

[9] C Dumouchel. Liquid Atomization and Spray: A Multi-Scale Description. volume Proceedings of the ASME 2017 of *Fluids Engineering Division Summer Meeting*, 07 2017.

[10] C Dumouchel, W Aniszewski, T-T Vu, and T Ménard. Multi-scale analysis of simulated capillary instability. *Int. J. Multiphase Flow*, 92:181–192, 2017.

[11] C Dumouchel and S Grout. Application of the scale entropy diffusion model to describe a liquid atomization process. *International Journal of Multiphase Flow*, 35(10):952–962, 2009.

[12] B Duret, J Reveillon, T Menard, and FX Demoulin. Improving primary atomization modeling through dns of two-phase flows. *International Journal of Multiphase Flow*, 55:130–137, 2013.

[13] M Essadki, F Drui, A Larat, T Ménard, and M Massot. Statistical modeling of the gas–liquid interface using geometrical variables: Toward a unified description of the disperse and separated phase flows. *Int. J. Multiphase Flow*, 120:103084, 2019.

[14] Herbert Federer. Curvature measures. *Transactions of the American Mathematical Society*, 93(3):418–491, 1959.

[15] R P Fedkiw, T Aslam, B Merriman, and S Osher. A non-oscillatory eulerian approach to interfaces in multimaterial flows (the ghost fluid method). *J Comput Phys*, 152(2):457–492, 1999.

[16] Malcolm J Grimson. Small-angle scattering from colloidal dispersions. *J. Chem. Soc.*, 79(6):817–832, 1983.

[17] Norbert Kleinjohann. Convexity and the unique footpoint property in riemannian geometry. *Archiv der Mathematik*, 35(1):574–582, 1980.

[18] AH Lefebvre and VG McDonell. *Atomization and Sprays*. CRC Press, Taylor and Francis Group, 2017.

[19] Jiacai Lu and Gretar Tryggvason. Direct numerical simulations of multifluid flows in a vertical channel undergoing topology changes. *Physical Review Fluids*, 3(8):084401, 2018.

[20] Jiacai Lu and Gretar Tryggvason. Multifluid flows in a vertical channel undergoing topology changes: Effect of void fraction. *Physical Review Fluids*, 4(8):084301, 2019.

[21] H Mantz, K Jacobs, and K Mecke. Utilizing minkowski functionals for image analysis: a marching square algorithm. *J. Stat. Mech: Theory Exp.*, 2008(12):P12015, 2008.

[22] G. Matheron. La formule de steiner pour les érosions. *Journal of Applied Probability*, 15(1):126–135, 1978.

[23] Klaus R Mecke. The shape of parallel surfaces: Porous media, fluctuating interfaces and complex fluids. *Physica A*, 314(1-4):655–662, 2002.

[24] T Ménard, S Tanguy, and A Berlemont. Coupling level set/VOF/ghost fluid methods: Validation and application to 3D simulation of the primary break-up of a liquid jet. *Int. J. Multiphase Flow*, 33(5):510–524, 2007.

[25] L Palanti, S Puggelli, L Langone, A Andreini, J Reveillon, Benjamin Duret, and FX Demoulin. An attempt to predict spray characteristics at early stage of the atomization process by using surface density and curvature distribution. *International Journal of Multiphase Flow*, 147:103879, 2022.

[26] M Rudman. A volume-tracking method for incompressible multifluid flows with large density variations. *Int J Numer Methods Fluids*, 28(2):357–378, 1998.

[27] CM Sorensen. Light scattering by fractal aggregates: a review. *Aerosol Science & Technology*, 35(2):648–687, 2001.

[28] M Sussman, KM Smith, MY Hussaini, M Ohta, and R Zhi-Wei. A sharp interface method for incompressible two-phase flows. *J Comput Phys*, 221(2):469–505, 2007.

[29] Mark Sussman, Peter Smereka, and Stanley Osher. A level set approach for computing solutions to incompressible two-phase flow. *J. Comput. Phys.*, 114(1):146 – 159, 1994.

[30] Max Teubner. Scattering from two-phase random media. *The Journal of chemical physics*, 92(7):4501–4507, 1990.

[31] F Thiesset, C Dumouchel, and T Ménard. A new theoretical framework for characterizing the transport of liquid in turbulent two-phase flows. In *ILASS-Europe, Paris*, 2019.

[32] F Thiesset, C Dumouchel, and T Ménard. Space/scale/time dynamics of liquid-gas shear flow. *J. Fluid Mech.*, 912(A39), 2021.

[33] F Thiesset, C Dumouchel, T Ménard, W Aniszewski, G Vaudor, and A Berlemont. Probing liquid atomization using probability density functions, the volume-based scale distribution and differential geometry. In *ILASS-Europe, Paris*, 2019.

[34] F Thiesset, B Duret, T Ménard, C Dumouchel, J Reveillon, and FX Demoulin. Liquid transport in scale space. *J. Fluid Mech.*, 886:A4, 2020.

[35] Albert Y Tong and Zhaoyuan Wang. Relaxation dynamics of a free elongated liquid ligament. *Phys Fluids*, 19(9):092101, 2007.

[36] S. Torquato. *Random Heterogeneous Materials. Microstructure and Macroscopic Properties*. Springer-Verlag New York, 2002.

[37] Gretar Tryggvason and Jiacai Lu. Characterizing the dynamics of complex multifluid flows undergoing topology changes. In *APS Division of Fluid Dynamics Meeting Abstracts*, pages H03–011, 2019.

[38] G Vaudor, T Ménard, W Aniszewski, M Doring, and A Berlemont. A consistent mass and momentum flux computation method for two phase flows. application to atomization process. *Computers Fluids*, 152:204–216, 2017.

[39] Trung-Thanh Vu and Christophe Dumouchel. Analysis of ligamentary atomization of highly perturbed liquid sheets. *International Journal of Multiphase Flow*, 107:156–167, 2018.

[40] CE Weatherburn. *Differential geometry of three dimensions*. Cambridge University Press, 1955.

[41] Hermann Weyl. On the volume of tubes. *American Journal of Mathematics*, 61(2):461–472, 1939.

[42] J Zhang. Acceleration of five-point red-black gauss-seidel in multigrid for poisson equation. *Appl. Math. Comput.*, 80(1):73–93, 1996.

Appendix A. Derivation of the classical Steiner formula

Geometric measures of parallel sets are well described for C^2-class surfaces (for which differential geometry applies) and C^0-class convex sets (using results from integral geometry). Before we start, it is necessary to describe the convention used throughout the present work.

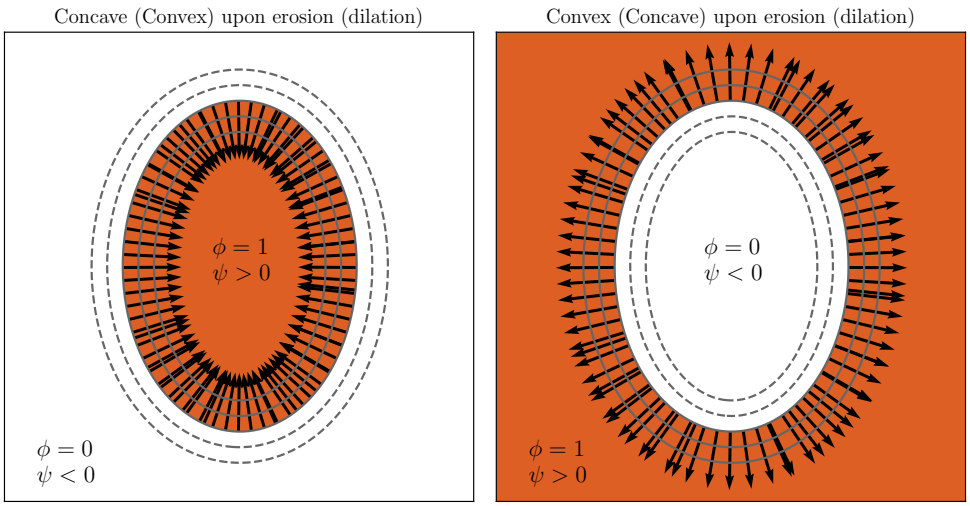

Figure A.18: Sketch portraying the convention used in the present study. The phase indicator function $\phi = 1$ in the phase of interest (here the liquid phase) and zero elsewhere. The normal to the interface $\boldsymbol{n} = \boldsymbol{\nabla}\phi$ are represented by arrows. The interfaces obtained upon erosion operations are displayed by full lines. Those obtained from dilation are shown by dashed lines. On the left figure, the normals are pointed towards each others, hence the structure is concave upon erosion but convex upon dilation. The opposite applies to the complement object sketched in the right figure.

Appendix A.1. Convention

Let us define the phase indicator function $\phi(\boldsymbol{x}) = 1$ in the phase of interest (here the liquid phase) and zero elsewhere (see Fig. A.18). The set of points where $\phi = 1$ is noted $A = \{\boldsymbol{x} \mid \phi(\boldsymbol{x}) = 1\}$.

The bodies A_{dil} and A_{ero} obtained by either a dilation or an erosion operation are characterized by the Minkowski addition (noted $\oplus$) and subtraction (noted $\ominus$), respectively

$$A_{\text{dil}} = A \oplus B_{d/2} \tag{A.1a}$$
$$A_{\text{ero}} = A \ominus B_{d/2} = (A^c \oplus B_{d/2})^c \tag{A.1b}$$

Here, $B_{d/2}$ is a spherical structural element of radius $d/2$ and the superscript c denotes the complement body, i.e. $A^c = \{\boldsymbol{x} \mid \phi(\boldsymbol{x}) = 0\}$

We further set the normal vector $\boldsymbol{n}$ to the interface separating zones where $\phi(\boldsymbol{x}) = 1$ and $\phi(\boldsymbol{x}) = 0$ as $\boldsymbol{n} = \boldsymbol{\nabla}\phi$. Therefore, $\boldsymbol{n}$ points towards zones where $\phi(\boldsymbol{x}) = 1$ (see Fig. A.18). The objects obtained by successive erosion and dilation operations form an infinite set of parallel bodies which can further be defined by:

$$A_{\text{dil}} = \{\boldsymbol{x} \mid \psi(\boldsymbol{x}) \geq -d/2\} \tag{A.2a}$$
$$A_{\text{ero}} = \{\boldsymbol{x} \mid \psi(\boldsymbol{x}) \geq d/2\} \tag{A.2b}$$

where $\psi(\boldsymbol{x})$ is the signed distance function from the interface which is positive in zones where $\phi(\boldsymbol{x}) = 1$ (in the direction of $\boldsymbol{n}$) and negative elsewhere. In other words, $d/2 > 0$ (in the $\boldsymbol{n}$ direction) corresponds to erosion and $d/2 < 0$ to dilation. The interfaces obtained by erosion and dilation operations are portrayed in Fig. A.18 as full and dashed lines, respectively. It is worth stressing that if, locally, the normals are converging towards each other, i.e. $\boldsymbol{\nabla} \cdot \boldsymbol{n} < 0$ (left panel of Fig. A.18), then the body is seen as being convex upon dilation but concave upon erosion. On the contrary, when normals are diverging, i.e. $\boldsymbol{\nabla} \cdot \boldsymbol{n} > 0$ (right panel of Fig. A.18), the body is convex upon erosion and concave upon dilation.

Appendix A.2. C^2-class surface

We use intrinsic coordinates to characterize the surface. Let ξ_1 and ξ_2 be the intrinsic surface coordinates attached to a surface noted $\mathcal{S}(0)$ at point $\boldsymbol{p}(0)$ and aligned with the principal directions of curvature. Let $\boldsymbol{e}_1$ and $\boldsymbol{e}_2$ denote the unit vector tangential to the parametric curves $\xi_{1,2} = \text{const}$. Then $\boldsymbol{n} = \boldsymbol{e}_1 \times \boldsymbol{e}_2$ is the unit normal vector to $\mathcal{S}(0)$. $(\boldsymbol{e}_1, \boldsymbol{e}_2, \boldsymbol{n})$ forms an orthogonal triad of unit vectors attached to $\mathcal{S}(0)$ at point $\boldsymbol{p}(0)$ as represented in Fig. A.19.

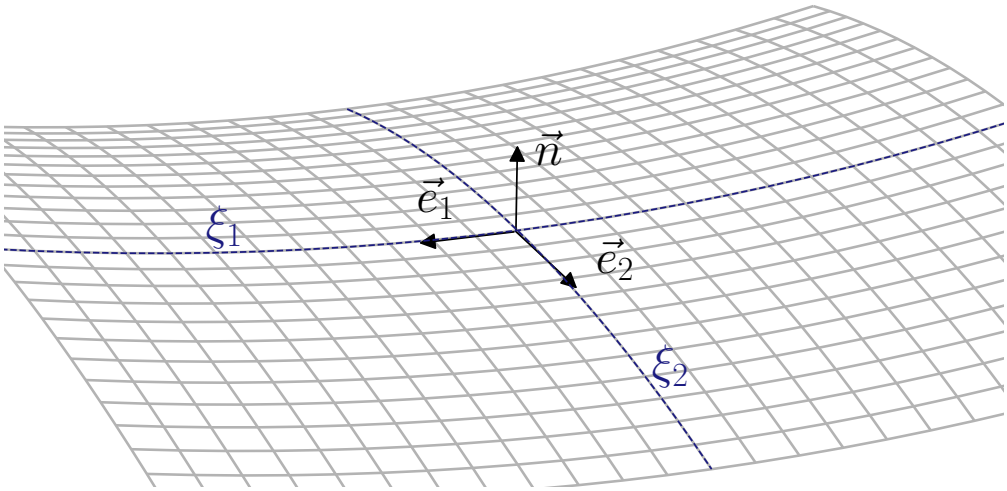

Figure A.19: Synthetic representation of the intrinsic curvilinear coordinate system attached to the surface $\mathcal{S}(0)$ at a given point $\boldsymbol{p}(0)$

A surface $\mathcal{S}(d)$, which is at constant distance $d/2$ along the normal of $\mathcal{S}(0)$, is said to be parallel to $\mathcal{S}(0)$. We also refer the parallel surface $\mathcal{S}(d)$ to as the eroded system at distance $d/2$. Then the point $\boldsymbol{p}(d)$ is related to $\boldsymbol{p}(0)$ by

$$\boldsymbol{p}(d) = \boldsymbol{p}(0) + \frac{d}{2}\boldsymbol{n} \tag{A.3}$$

Eq. (A.3) serves as a transformation that relates the Cartesian coordinates (x_1, x_2, x_3) to the new coordinate system, and can be inverted to express (ξ_1, ξ_2, d) in terms of (x_1, x_2, x_3). In particular, the elementary volume d^3V between two parallel surfaces separated by a distance $\frac{d}{2}$ can be expressed as

$$\mathrm{d}^3V = h_1 h_2 h_3 \ \mathrm{d}\xi_1 \mathrm{d}\xi_2 \mathrm{d}\frac{d}{2} \tag{A.4}$$

where the scale factors or Lamé coefficients write [40, p.158]:

$$h_1 = 1 + \frac{d}{2}\kappa_1(0) \tag{A.5a}$$

$$h_2 = 1 + \frac{d}{2}\kappa_2(0) \tag{A.5b}$$

$$h_3 = 1 \tag{A.5c}$$

Here $\kappa_1(0)$ and $\kappa_2(0)$ are the principal curvature of $\mathcal{S}(0)$ at point $\boldsymbol{p}(0)$ in the ξ_1- and ξ_2-directions, respectively. Hence, the elementary volume between two parallel surfaces separated by a distance $\frac{d}{2}$, viz.

$$\begin{aligned} \mathrm{d}^3V &= \frac{1}{2}\left[1 + \kappa_1(0)\frac{d}{2}\right]\left[1 + \kappa_2(0)\frac{d}{2}\right]\mathrm{d}\xi_1\mathrm{d}\xi_2\mathrm{d}d \\ &= \frac{1}{2}\left[1 + \mathcal{H}(0)d + \mathcal{G}(0)\frac{d^2}{4}\right]\mathrm{d}\xi_1\mathrm{d}\xi_2\mathrm{d}d \end{aligned} \tag{A.6}$$

with $2\mathcal{H}(0) = \kappa_1(0) + \kappa_2(0)$ and $\mathcal{G}_0 = \kappa_1(0)\kappa_2(0)$. $\mathcal{H}(0)$ and $\mathcal{G}(0)$ are respectively the mean and Gaussian curvature of $\mathcal{S}(0)$ at $\boldsymbol{p}(0)$. The volume $V(d)$ of the eroded system a distance $d/2$ then writes

$$\begin{aligned} V(d) &= V(0) - \\ &\quad \frac{1}{2}\int_{\xi_1}\int_{\xi_2}\int_0^d (1 + \mathcal{H}(0)\delta + \mathcal{G}(0)\frac{\delta^2}{4})\mathrm{d}\xi_1\mathrm{d}\xi_2\mathrm{d}\delta \\ &= V(0) - S(0)\frac{d}{2}\left[1 + \langle\mathcal{H}(0)\rangle\,\frac{d}{2} + \langle\mathcal{G}(0)\rangle\,\frac{d^2}{12}\right] \end{aligned} \tag{A.7}$$

where

$$S(0) = \int_{\xi_1} \int_{\xi_2} \mathrm{d}\xi_1 \mathrm{d}\xi_2 \tag{A.8}$$

is the surface area of $\mathcal{S}(0)$ and $\langle\ \rangle$ denotes the area weighted average over $\mathcal{S}(0)$, i.e.

$$\langle \bullet(0) \rangle = \frac{1}{S(0)} \int_{\xi_1} \int_{\xi_2} \bullet(0)\ \ \mathrm{d}\xi_1 \mathrm{d}\xi_2 \tag{A.9}$$

Eq. (A.9) can be written for any quantities at any distance from the interface $d/2$. For the sake of clarity, we define

$$H(0) = \langle \mathcal{H}(0) \rangle S(0) \tag{A.10a}$$
$$G(0) = \langle \mathcal{G}(0) \rangle S(0) \tag{A.10b}$$

similarly,

$$H(d) = \langle \mathcal{H}(d) \rangle S(d) \tag{A.11a}$$
$$G(d) = \langle \mathcal{G}(d) \rangle S(d) \tag{A.11b}$$

Using this notation, Eq. (A.7) can be rewritten as:

$$V(d) = V(0) - S(0)\frac{d}{2} - H(0)\frac{d^2}{4} - G(0)\frac{d^3}{24} \tag{A.12}$$

Although slightly different, this expression is closely related to the Weyl's tube formula [41].

Differential geometry further allows us to write an expression for the area $S(d)$ of the parallel surface $\mathcal{S}(d)$ at a distance $d/2$ from $\mathcal{S}(0)$

$$S(d) = S(0) + H(0)d + G(0)\frac{d^2}{4} \tag{A.13}$$

For the principal curvature, we have [40, p.159]

$$\kappa_i(d) = \frac{\kappa_i(0)}{1 + \kappa_i(0)\frac{d}{2}} \tag{A.14}$$

with $i = 1, 2$. Hence, the mean and Gaussian curvatures of $\mathcal{S}(d)$ write

$$\mathcal{H}(d) \quad = \quad \frac{\mathcal{H}(0) + \mathcal{G}(0)\frac{d}{2}}{1 + \mathcal{H}(0)d + \mathcal{G}(0)\frac{d^2}{4}} \tag{A.15a}$$
$$\mathcal{G}(d) \quad = \quad \frac{\mathcal{G}(0)}{1 + \mathcal{H}(0)d + \mathcal{G}(0)\frac{d^2}{4}} \tag{A.15b}$$

Proceeding to surface area weighted average yields

$$H(d) \quad = \quad H(0) + G(0)\frac{d}{2} \tag{A.16a}$$
$$G(d) \quad = \quad G(0) \tag{A.16b}$$

As a consequence, the volume $V(d)$, the surface area $S(d)$, mean $H(d)$ and Gaussian curvatures $G(d)$ are simply related by:

$$-2V(d)_{,d} \quad = \quad S(d) \tag{A.17a}$$
$$S(d)_{,d} \quad = \quad H(d) \tag{A.17b}$$
$$2H(d)_{,d} \quad = \quad G(d) \tag{A.17c}$$

where Einstein notation has been used for derivatives w.r.t d, i.e.

$$\bullet_{,x} = \frac{\partial}{\partial x} \bullet \tag{A.18}$$

where x denotes either the scale d or time t. It is also worth introducing the Euler characteristic $\chi(d)$ which by virtue of the Gauss-Bonnet theorem writes

$$\chi(d) = G(d)/2\pi \tag{A.19}$$

Appendix A.3. C^0-class surface

When the surface possesses singular edges and corners (e.g. a triangulated surface), differential geometry does not apply. Nevertheless, integral geometric measures for the volume V, the surface area S and curvatures H, G can still be defined.

For convex-sets in 3D space, the volume of the eroded system $V(d)$ can be expressed using Steiner's formula [22]:

$$V(d) = \sum_{\nu=0}^{3} \binom{3}{\nu} \omega_\nu V_\nu(0) \left(-\frac{d}{2}\right)^\nu \tag{A.20}$$

where

$$\binom{n}{p} = \frac{n!}{p!(n-p)!} \tag{A.21}$$

ω_ν denotes the ν-dimensional volume of a unit-sphere, i.e. $\omega_0 = 1$, $\omega_1 = 2$, $\omega_2 = \pi$ and $\omega_3 = 4\pi/3$ and the V_ν are called the Minkowski functional (abbreviated MF) and are given by

$$V_0 = V, \tag{A.22a}$$
$$6V_1 = S, \tag{A.22b}$$
$$3\pi V_2 = -H \tag{A.22c}$$
$$4\pi V_3 = G \tag{A.22d}$$

In general, the Minkowski functional $V_\nu(d)$ of the eroded parallel set are given by [22]:

$$V_\nu(d) = \sum_{\mu=0}^{3-\nu} \binom{3-\nu}{\mu} \frac{\omega_{\nu+\mu}}{\omega_\nu} V_{\nu+\mu}(0) \left(-\frac{d}{2}\right)^\mu \tag{A.23}$$

Eq. (A.23) yields the same expression for the volume $V(d)$, surface area $S(d)$, mean $H(d)$ and Gaussian curvatures $G(d)$ as Eqs. (A.12), (A.13), (A.16a) and (A.16b), respectively. The same applies to Eqs. (A.17). In summary, irrespectively of the type of surface (C^2 or C^0-convex), the relations for the volume, surface area and curvatures of the eroded system are the same. For C^2-class, they are generally referred to as the Weyl's formula while for C^0-convex sets, they are called the Steiner's formula.

If one considers a dilation operation instead of an erosion, these equations applies simply by inverting the scale $d/2$.

Appendix B. Derivation of the corrected Steiner formula

Appendix B.1. Sets of finite reach

Eqs. (A.12), (A.13), (A.16a) and (A.16b) reveal that integral geometric measures of the parallel body are uniquely determined by the ones at zero dilation/erosion. Further, Eqs. (A.17) proves that by knowing only e.g. the volume $V(d)$, one can obtain all others Minkowski functional by simple derivations w.r.t d.

Eqs. (A.12), (A.13), (A.16a) and (A.16b) remain valid as long as all points on $\mathcal{S}(d)$ possesses a unique correspondent on $\mathcal{S}(0)$, that is to say when the value of $d/2$ is less than the reach. Depending on the morphological operation (dilation or dilation) and the convexity of the body upon such an operation, one may define the erosion reach and/or the dilation reach.

All convex bodies (which by definition have infinite reach), and all bodies with C^2-class boundary fall within the class of sets with positive reach [14]. In other words, the notion of set with positive reach (or unique footprint [17]) is a generalization that embeds both convex and C^2-class surfaces.

For non-convex bodies and for C^2-class sets at erosion scales larger than the reach, there are, to the best of our knowledge, no known measurable relations similar to Eqs. (A.12), (A.13), (A.16a) (A.16b), and (A.17).

In what follows, we aim at extending the analysis by deriving relations similar to Eqs. (A.17) which hold for non-convex sets beyond the reach. In this perspective, we also hope providing insights into the link between integral geometrical measures of the body under consideration and what [2] refer to as 'non-local' properties. For the analysis to be analytically tractable, we will consider only simple shapes: tubular bodies, systems of revolution with linear or circular medial axis.

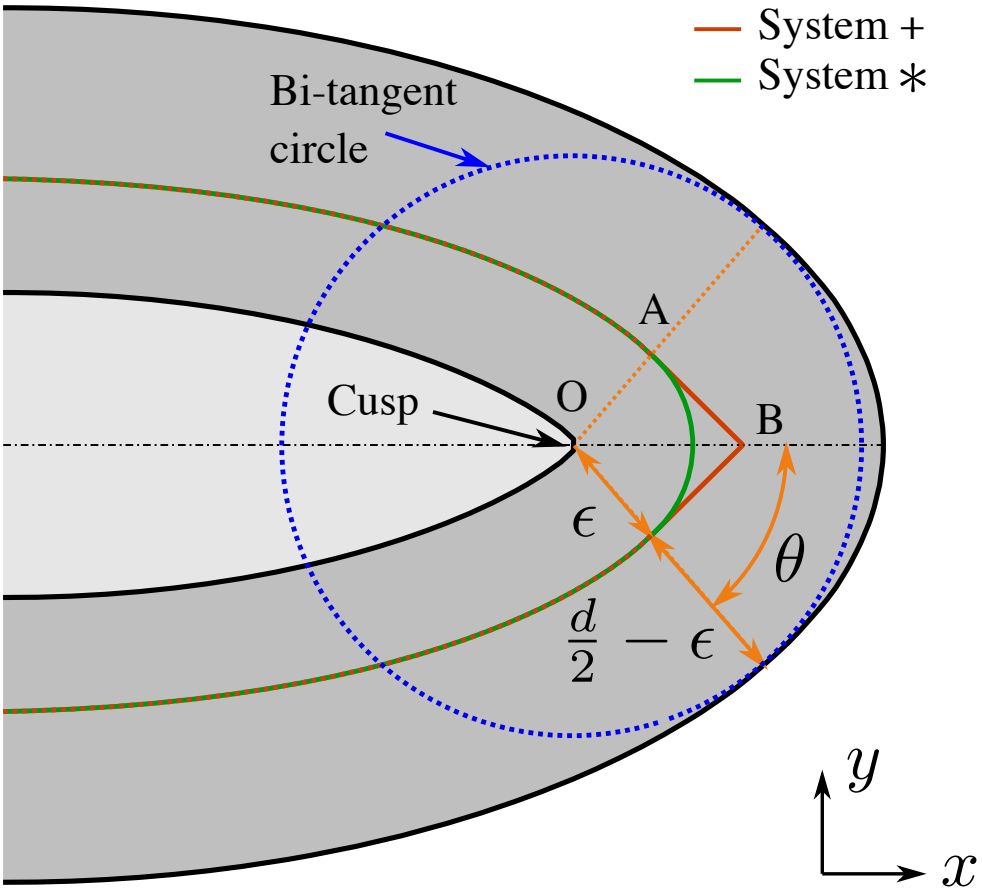

Figure B.20: Schematic of a body yielding the formation of a cusp when eroded at a scale $d/2 >$ reach.

A system eroded at a scale $d/2$ larger than the reach presents at least one cusp, a local singularity located on the medial axis at a distance $d/2$ from the original system boundary. As illustrated in Fig. B.20, $d/2$ is then the radius of the bi-tangent circle to the system boundary. The cusp is located at the center of this bi-tangent circle. For the ellipsoid of Fig. B.20 the medial axis lies on the horizontal axis. As demonstrated through the forthcoming analysis, the cusp plays a central role for characterizing non-convex bodies.

Let us define by a $+$ the system obtained after erosion of the original system at a scale $d/2 - \epsilon$ (the system delimited by the red curve in Fig. B.20), and by a $*$ the system obtained after erosion of the original system at a scale $d/2$ followed by a dilation at scale ϵ (the system delimited by the green curve in Fig. B.20).

The trick we employ to derive Steiner-type formula for erosion scales beyond the reach is based on the observation that the MFs of the systems $+$ and $*$ differ except in the limit $\epsilon \to 0$ where they are the same. For simple shapes, and given a realistic hypothesis on the system $+$, this difference and its limit as $\epsilon \to 0$ can be analytically computed. As we will see later in this section, this ultimately leads to corrections of Eqs (A.17). The aforementioned hypothesis on the system $+$ is to consider that the segment AB is tangent to the curve at point A and hence the triangle OAB is right-angle (i.e. $\boldsymbol{OA} \cdot \boldsymbol{AB} = 0$). By doing so, one can compute the MFs for both systems $*$ and $+$ as now described.

Appendix B.2. Extruded systems

We start by considering extruded systems. These are characterized by a fixed cross section in the plane xy that is simply repeated over the z axis (we use the same axis convention as in Fig. B.20). The extent of the body in the z directions is noted h. Note that such systems have zero Gaussian curvature. Proceeding with the calculation of volume, surface area, mean and Gaussian curvatures, for both $+$ and $*$ systems, one

obtains

$$V^+(\epsilon) = V^*(\epsilon) + h\epsilon^2(\tan\theta - \theta) \tag{B.1a}$$
$$S^+(\epsilon) = S^*(\epsilon) + 2h\epsilon(\tan\theta - \theta) \tag{B.1b}$$
$$H^+(\epsilon) = H^*(\epsilon) \tag{B.1c}$$
$$\chi^+(\epsilon) = \chi^*(\epsilon) = 0 \tag{B.1d}$$

Steiner's formula applies to the system $*$ for dilation at scale ϵ [2], viz.

$$V^*(\epsilon)_{,\epsilon} = S^*(\epsilon) \tag{B.2a}$$
$$S^*(\epsilon)_{,\epsilon} = -2H^*(\epsilon) \tag{B.2b}$$
$$H^*(\epsilon)_{,\epsilon} = -2\pi\chi^*(\epsilon) \tag{B.2c}$$

In Eq. (B.2), derivatives are performed w.r.t ϵ. Using (B.1) and Eq. (B.2), one can show that

$$V^+(\epsilon)_{,\epsilon} = S^+(\epsilon) \tag{B.3a}$$
$$S^+(\epsilon)_{,\epsilon} = -2H^+(\epsilon) + 2h(\tan\theta - \theta) \tag{B.3b}$$
$$H^+(\epsilon)_{,\epsilon} = -2\pi\chi^+(\epsilon) \tag{B.3c}$$

The relations for the actual system upon erosion at scale $d/2$ is obtained by setting $d \equiv -2\epsilon$ in Eqs. (B.3) before applying the limit $\epsilon \to 0$). By doing so, we obtain:

$$2V(d)_{,d} = -S(d) \tag{B.4a}$$
$$S(d)_{,d} = H(d) - h(\tan\theta - \theta) \tag{B.4b}$$
$$2H(d)_{,d} = 2\pi\chi(d) \tag{B.4c}$$

Eqs. (B.4) indicate that an extra term is present in the expression for the mean curvature $H(d)$ while the relations pertaining to the surface area and Euler characteristic remain unchanged. This correction reads as the product of the cusp length (here h) by a correction factor which depends on the angle θ between the normal to the set boundary and the x axis (the axis on which the medial axis falls). θ depends on the scale $d/2$ and hence the correction is scale-dependent.

Appendix B.3. Axisymmetric systems with linear medial axis

Light is now shed on a Steiner type formula for an axisymmetric system whose medial axis reduces to a line. Such a system can be obtained by e.g. rotating Fig. B.20 around the x axis. Using the same procedure as in §Appendix B.2, we get

$$V^+(\epsilon) = V^*(\epsilon) + 2\pi\frac{(1-\cos\theta)^2}{\cos\theta}\frac{\epsilon^3}{3} \tag{B.5a}$$
$$S^+(\epsilon) = S^*(\epsilon) + 2\pi\frac{(1-\cos\theta)^2}{\cos\theta}\epsilon^2 \tag{B.5b}$$
$$H^+(\epsilon) = H^*(\epsilon) - 2\pi\frac{(1-\cos\theta)^2}{\cos\theta}\epsilon \tag{B.5c}$$
$$\chi^+(\epsilon) = \chi^*(\epsilon) \tag{B.5d}$$

which, by virtue of Eqs. (B.2), yields

$$2V(d)_{,d} = -S(d) \tag{B.6a}$$
$$S(d)_{,d} = H(d) \tag{B.6b}$$
$$2H(d)_{,d} = 2\pi\chi(d) + 2\pi\frac{(1-\cos\theta)^2}{\cos\theta} \tag{B.6c}$$

It is worth emphasizing that for objects of revolution with a linear medial axis, the correction appears only on the Euler characteristics while the surface area and mean curvature remain untouched.

Appendix B.4. Axisymmetric systems with circular medial axis

A system similar to Fig. B.20 but rotated around the y axis possesses a circular medial axis. In this condition, one obtains

$$\begin{aligned} V^+(\epsilon) &= V^*(\epsilon) \quad +2\pi r_c(\tan\theta-\theta)\epsilon^2 \\ &\qquad\qquad +2\pi\tan^2\theta\sin\theta\frac{\epsilon^3}{3} && \text{(B.7a)} \\ S^+(\epsilon) &= S^*(\epsilon) \quad +4\pi r_c(\tan\theta-\theta)\epsilon \\ &\qquad\qquad +2\pi\tan^2\theta\sin\theta\epsilon^2 && \text{(B.7b)} \\ H^+(\epsilon) &= H^*(\epsilon) \quad -2\pi\left(\frac{\theta}{\cos\theta}-\sin\theta\right)\epsilon && \text{(B.7c)} \\ \chi^+(\epsilon) &= \chi^*(\epsilon) && \text{(B.7d)} \end{aligned}$$

where r_c is the radial distance of the cusp. Using again Eqs. (B.2), we can show that

$$\begin{aligned} 2V(d)_{,d} &= -S(d) && \text{(B.8a)} \\ S(d)_{,d} &= H(d)-2\pi r_c(\tan\theta-\theta) && \text{(B.8b)} \\ 2H(d)_{,d} &= 2\pi\chi(d)+2\pi\left(\frac{\theta}{\cos\theta}-\sin\theta\right) && \text{(B.8c)} \end{aligned}$$

Note here that the corrections appear on both the mean and Gaussian curvature while the relations for surface area remain the same as Eq. (A.17). As it was the case for extruded systems (Eq. (B.4)), the correction on the mean curvature reads as the product of the cusp length (here $2\pi r_c$) by $\tan\theta-\theta$.